BETA DECAY AND DEFORMATION.
STUDIES OF NEUTRON-RICH NUCLEI WITH 106≤A≤114

BY
ARI JOKINEN

Academic Dissertation
for the Degree of
Doctor of Philosophy

Jyväskylä, Finland
May 1994

BETA DECAY AND DEFORMATION.
STUDIES OF NEUTRON-RICH NUCLEI WITH 106≤A≤114

BY
ARI JOKINEN

Academic Dissertation
for the Degree of
Doctor of Philosophy

To be presented, by permission of the
Faculty of Mathematics and Natural Sciences
of the University of Jyväskylä,
for public examination in Auditorium S-212 of the
University of Jyväskylä on May 27, 1994,
at 12 o'clock noon

Jyväskylä, Finland
May 1994

Preface

It has been a privilege to work in the enthusiastic and inspiring atmosphere of the IGISOL-group. I am greatly indebted to the leader of the group and my supervisor, Prof. J. Äystö, for his guidance and support throughout the years. I would also like to thank for a pleasant collaboration the permanent members of the group, Ph.D. H. Penttilä, M.Sc. P. Jauho, M.Sc. J.-M. Parmonen and Ph.Lic. P. Taskinen, as well as the others who have worked with the group for shorter periods. I am grateful to Ass. Prof. K. Eskola and Dr. M. Leino for their contribution to most of these experiments and for their many valuable comments.

My thanks go also to the staff of the Department of Physics, University of Jyväskylä. I cannot mention everyone but I would like to single out Prof. P. Lipas, Dr. E. Hammaren, and Dr. J. Suhonen, whose lectures and guidance in the field of theoretical nuclear physics have broadened my horizons. I also want to express my gratitude to Mr. H. Leinonen. Without his patient operation of the old MC-20 cyclotron this thesis would not exist.

Several visitors have contributed to this work. I thank Prof. R. Beraud, Dr. C.N. Davids, Dr. P. Dendooven, Dr. Z. Janas, Prof. K.-L. Kratz, Dr. G. Lhersonneau, Dr. K. Rykaczewski and Prof. J. Zylicz for the enlightening discussions and excellent co-operation.

Financial support from the Academy of Finland made it possible for me to concentrate on the research work which is greatly appreciated.

Finally, my warmest thanks go to my beloved wife, Sirpa, for her endless support and encouragement.

Jyväskylä, May 1994

Ari Jokinen

Abstract

This thesis deals with beta decay studies conducted at the Department of Physics, University of Jyväskylä. The studied neutron rich nuclei with $106 \leq A \leq 114$ were produced in a proton induced fission of ^{238}U and they were mass separated by using an on-line mass separation facility IGISOL. In this thesis, the main emphasis has been put on the fundamental properties of beta decay in the wide range of nuclei from the deformed Zr-region to the almost spherical Pd-nuclei. These studies have produced new beta decay data in the region of interest and led to the identification of seven new isotopes. The obtained experimèntal information have been compared to the global models of atomic masses and beta decay rates. In addition, this thesis includes macroscopic-microscopic calculations for the beta decay properties as a function of deformation and nucleon number. The comparison of the experimental and calculated data have been used to extract information about the interplay between deformation and fundamental beta decay properties of the nuclei studied.

Table of Contents

1   Introduction

Research on nuclei far from stability has gained a lot of new interest due to the rapid development of the experimental techniques. The proton drip-line has been experimentally probed up to Bromium and the elements up to Neon have been identified on the neutron drip-line [Äys89,Det89,Han89,Roe92,Mue93]. Although a lot can be learned from the nuclei near the valley of beta stability, the nuclei far from stability, also called exotic nuclei, posses a special interest due to their extreme composition of the neutrons and protons. This provides a stringent test for the nuclear structure models, which often are formulated and parametrized according to information obtained from less exotic nuclei. For instance, the shell structure may reveal new insight when approaching the drip-line nuclei, as pointed out by M.M. Sharma *et al.* [Sha94] and J. Dobaczewski *et al.* [Dob94]. The first observation of the anomalous large total interaction cross section of the ^{11}Li and ^{6,8}He isotopes [Tan85] has resulted in a new branch of the nuclear physics, which is devoted to the study of neutron haloes associated with exceptionally large radii of neutron matter distribution [Tan91]. Although the exotic nuclei are rare in the stellar environment, they appear all the time in the universe at different stages of the evolution of stars. For instance, they play a major role in the synthesis of heavy elements via a r(apid neutron capture)-process [Kra93]. The abundance of the r-process nuclei is defined by the seed nucleus of the r-process path, temperature, neutron density and the time scale of the r-process. Nowadays an understanding of the various processes is limited to the degree to which the underlying nuclear physics data have been measured and understood. The most important nuclear physics input parameters are the decay rates λ, decay energies Q, neutron-capture cross sections σ_n and also the shape of the beta-strength function S_β [Thi91].

The aim of this work is to gather new experimental information concerning the beta decay properties for neutron-rich nuclei in the transitional region from strongly deformed Zirconium-nuclei to almost spherical Palladium-nuclei. The region of interest is highly exciting due to the experimental observations, like shape-coexistence [Lhe93], identical bands [Lhe90] and rich isomerism [Pen92,Fog90] among many others. An increasing distance from the stability line leads to increasing Q-values of beta decay. This provides powerful tool for the experimental studies of nuclear β decay. In neutron-rich nuclei, the allowed beta decay is of the Gamow Teller type due to unfavorable energetics for the Fermi-transition.

According to an extreme single particle shell model (ESPSM), one valence nucleon outside the inert core is responsible for the allowed beta decay between the initial and final states. In the case of the GT-beta decay of an even-even parent nucleus, a spin and a parity of the final state is uniquely defined as 1$^+$ due to the selection rules of allowed beta decay. For the neutron-rich nuclei with $40 \leq Z \leq 50$, the ESPSM-model should result in only one 0$^+\rightarrow$1$^+$

1

transition, which occurs between the spin-orbit partners $\nu g_{7/2}$ and $\pi g_{9/2}$. An illustrative example of that is the decay of $^{124\text{-}128}$Cd-isotopes, which reveal one strong $0^+ \rightarrow 1^+$ beta transition. This is demonstrated in Fig. 1.1, which shows the partial decay schemes of $^{124\text{-}128}$Cd according to [Spa87]. The situation is quite different already for Pd-isotopes, whose decays indicate the effects of configuration mixing and residual interactions [Kop89,Fog90,Jan93].
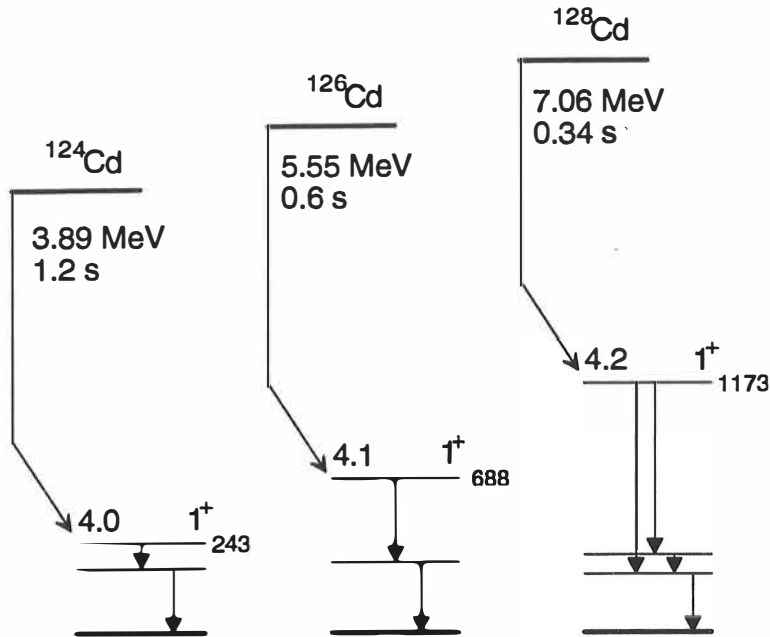
Figure 1.1 Partial decay schemes of $^{124\text{-}128}$Cd-isotopes [Spa87]. Log ft values of $0^+ \rightarrow 1^+$ beta transitions and the energies of the final states are illustrated.

In nuclei out of the closed shells, the ESPSM-model is far too simple, as was exemplified already in the case of the Pd-isotopes. When the distance from the nearest closed shell is further increased the deformation of the nucleus starts to play an important role. In the single-particle picture this means that spherical shell model states are split according to different m-values. These are strongly mixed when associated to small deformation. In the well deformed regions, the single-particle states are fully characterized by the asymptotic quantum numbers N, n_z, Λ, and Σ. The selection rules of the asymptotic quantum numbers for the allowed beta decay are determined by G. Alaga [Ala55]. Among the allowed beta-transitions, the transitions fulfilling the selection rules $[\Delta N, \Delta n_z, \Delta \Lambda, \Delta \Sigma] = [0000]$ are called allowed unhindered (au) transitions. They are characterized by the low log ft values, i.e. log ft $\leq$ 5. The au-transitions

are systematically studied in the rare-earth region [Soo89,Soo90,Mei76,Zyl66]. In addition, there exist also some non-conclusive evidence for the au-transitions in actinides [Soo92].

Although the beta decay can be well understood at the asymptotic extremes, related with spherical or large deformation, the regions between these two extremes are puzzling as far as beta decay is concerned. The choice of the quantum numbers, the composition of the individual single-particle states and the identification of the single-particle states involved in beta decay are only few examples of the unresolved questions. In addition, the shape co-existence and the asymmetric shapes can greatly complicate the treatment of the beta decay in transitional regions. The collective properties of the nuclei affect directly the beta decay rates via the nuclear matrix element and pairing correlations. The change of deformation between the initial and the final state may result in poor overlap of the wave functions involved in beta decay. This in turn results in a hindrance of the beta decay. The deformed core also affects the occupation of the single-particle levels, which changes the pairing correction accordingly.

A strength of the Gamow Teller beta decay transition can be written as [Tow85]

$$B(\text{GT}) = \frac{C}{\left(g_A/g_V\right)^2 ft},\tag{1.1}$$

where f is a fermi function, t is a partial beta half-life and the strength $B(\text{GT})$ is proportional to the square of the intrinsic matrix element of the beta decay between the initial and the final state. According to this equation it is possible to obtain information about the beta decay matrix element and the coupling constants by measuring the half-life and the decay energy and constructing the decay scheme.

In this thesis the first step towards a better understanding of the beta decay in the transitional Zr-to-Pd-region has been taken by deducing the experimental observables: the decay energy, half-life and decay scheme of the neutron-rich Mo and Ru isotopes. These are then compared to various models, some of which are devoted to predict the atomic masses and half-lives.

This thesis is based on the experimental studies conducted at the Department of Physics of the University of Jyväskylä in 1989-1991. The bulk of the experiments was carried out in the spring 1991 and concluded by the last experiment in August 1991, just before closing the old MC-20 cyclotron. The experiments were undertaken as a part of the systematic program for the study of the neutron-rich transitional nuclei with A=100-120 at the IGISOL-facility. In this thesis, I concentrate on the beta decay properties of these nuclei. The special interest is in the connections between the deformation and beta decay characteristics. Figure 1.2 presents the section of the nuclide chart where the isotopes of this study are situated.

3
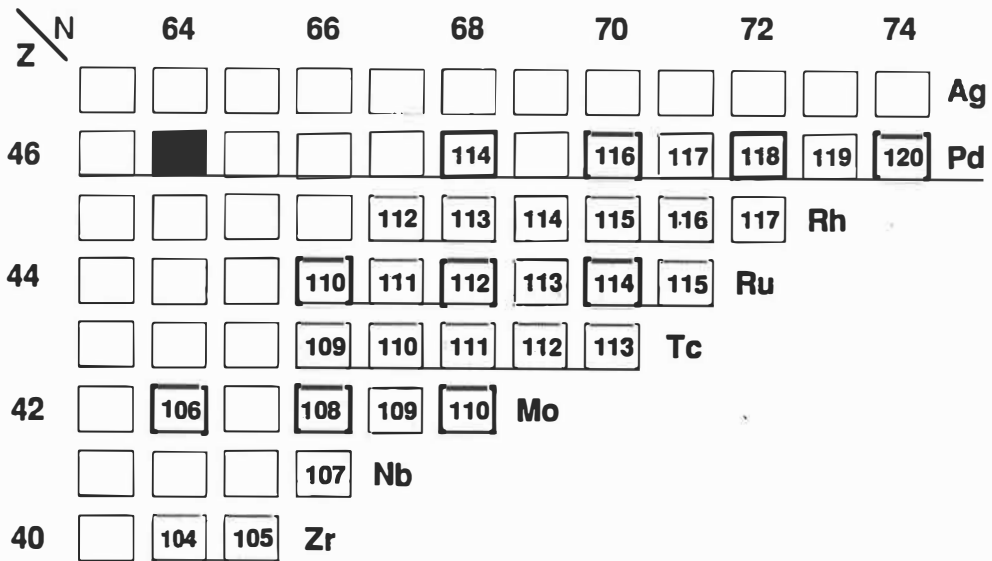
Figure 1.2 The chart of nuclides showing the neutron-rich transitional region with A≈100-120. The isotopes, which are studied at the IGISOL-facility are shaded. Those even-A isotopes, which are studied in this thesis, are framed with a thick solid line.

1.1 List of publications

This thesis is mostly based on the following articles:

I.   A. Jokinen, J. Äystö, P. Dendooven, K. Eskola, Z. Janas, P.P. Jauho, M.E. Leino, J.M. Pannonen, H. Penttilä, K. Rykaczewski and P. Taskinen, *Spin-flip β⁻ decay of even-even deformed nuclei ^{110}Ru and ^{112}Ru,* Zeitschrift für Physik **A340** (1991) 21-28. https://doi.org/10.1007/BF01284476

II.   J. Äystö, A. Astier, T. Enqvist, K. Eskola, Z. Janas, A. Jokinen, K.-L. Kratz, M. Leino, H. Penttilä, B. Pfeiffer and J. Zylicz, *Discovery of Rare Neutron-rich Zr, Nb, Mo. Tc, and Ru Isotopes in Fission: Test of β Half-Life Predictions Very Far from Stability,* Physical Review Letters **69** (1992) 1167-1170. Phttps://doi.org/10.1103/PhysRevLett.69.1167

III. A. Jokinen, J. Äystö, P.P. Jauho, M. Leino, J.M. Pannonen, H. Penttilä, K. Eskola and Z. Janas, *Beta decay of ^{114}Ru and Q_β systematics for n-rich Ru isotopes,* Nuclear Physics **A549** (1992) 420-430. https://doi.org/10.1016/0375-9474(92)90088-2

IV.   A. Jokinen, J. Äystö, K. Eskola, T. Enqvist, Z. Janas, P.P. Jauho, M. Leino, J.M. Pannonen, H. Penttilä and J. Zylicz, *New neutron-rich isotopes in the zirconium-to-palladium region; Gamow-Teller decay of deformed nuclei,* Inst. Phys. Conf. Ser. No 132: Section 5, 563-568. Paper presented at 6th International Conference on Nuclei Far From Stability & 9th International Conference on Atomic Masses and Fundamental Constants, Bernkastel-Kues, Germany, 1992.

V.   A. Jokinen, P.P. Jauho, T. Enqvist, K. Eskola, M. Leino, J.M. Pannonen, H. Penttilä, and J. Äystö, *Beta decay of ^{108}Mo and of neighbouring even Mo-isotopes,* JYFL Preprint No. 10/94, submitted for publication to Nuclear Physics A. https://doi.org/10.1016/0375-9474(94)00524-Q

In all articles mentioned above, the author of this thesis has been the main contributor except in Paper II. The author has set up the experiments and has been the responsible person in the analysis and interpretation of the data.

The main experimental results which are presented in Papers I-V have been summarized in chapter 4. Otherwise, the main emphasis is put on both the theoretical and technical details, which are often omitted in the original articles. The experimental results are discussed more extensively applying new aspects not included in the discussions of Papers I-V.

2 Theoretical background

2.1 Beta decay and the shell model

2.1.1 Kinematics of beta decay

Beta decay process is a three body problem of an electron, a neutrino and a participating nucleus, which greatly complicates its handling. However, the situation can be simplified due to the large rest mass of the nucleus compared to typical energies released in the beta decay. The mass of the nucleus can be approximated as infinite and the problem reduces to two body problem of the neutrino and electron [Beh82]. In that case the total energy release in the β^- decay, for example, is divided among the antineutrino and electron

$$E_0 = E_{\bar{\upsilon}} + E_{e^-}. \tag{2.1}$$

This formula can be transformed to the kinetic energies by subtracting the electron mass from both sides of the equation, leading to an equation

$$T_0 = T_{\upsilon} + T_{e^-}. \tag{2.2}$$

Due to the simultaneous emission of the antineutrino, the electron spectrum has a continuum-like shape, which is described in the allowed case by the formula

$$N(p) = \frac{C}{c^2} p^2 (Q - T_e)^2. \tag{2.3}$$

In addition, the shape of the beta spectrum is influenced by the Coulomb interaction between the nucleus and the emitted electrons and also by the contribution of the nuclear matrix element. This leads to the equation

$$N(p) \propto p^2 (Q - T_e)^2 F(Z, T_e) |M_{if}|^2 S(p, q), \tag{2.4}$$

where $p^2 (Q - T_e)^2$ is a statistical factor and $F(Z, T_e)$ is Fermi-function, which is tabulated for each element as a function of the kinetic energy of the emitted beta-particles [Gov71].

2.1.2 Conservation laws in beta decay

Emission of the electron and neutrino involves a possibility of the change of angular momentum L. Depending on whether the participating electron and the neutrino have their spins anti parallel or parallel, the transition is called Fermi (F) or Gamow-Teller (GT), respectively. Due to the conservation law of the angular momentum, the following equations of the vector additions hold in the two types of the beta transitions:

$$\mathbf{I}_f = \mathbf{I}_i + \mathbf{L} \qquad \text{Fermi transitions} \tag{2.5a}$$

$$\mathbf{I}_f = \mathbf{I}_i + \mathbf{L} + 1 \qquad \text{Gamow-Teller transitions} \tag{2.5b}$$

Additionally, the parities of the initial and final states are related in the following way:

$$\pi_i = \pi_f (-1)^L \tag{2.5c}$$

The selection rules for the change of the angular momentum and parity for different type of beta-transitions are summarized in the Table 2.1.

Table 2.1 The selection rules of the beta-transitions [Coh71].

Transition type	L	Fermi ΔI	Fermi $\Delta \pi$	Gamow-Teller ΔI	Gamow-Teller $\Delta \pi$
Allowed	0	0	No	(0),1	No
First forbidden	1	(0),1	Yes	0,1,2	Yes
Second forbidden	2	(1),2	No	2,3	No
Third forbidden	3	(2),3	Yes	3,4	Yes
Fourth forbidden	4	(3),4	No	4,5	No

2.1.3 Classification of beta transitions

A decay constant of the allowed beta decay can be written

$$\lambda = \frac{64\pi^4 g^2 \left| M_{if} \right|^2}{h^7 c^3} \int_0^{p_{max}} F(Z,p) p^2 (Q - T_e)^2 \, dp. \tag{2.6}$$

The integral of the equation above is normally given as a function $f(Z,Q\text{-}E)$, which is known as a Fermi-integral. By taking $\lambda = \ln 2 / T_{1/2}$, following formula for the relation of the beta decay rate and the transition probability is obtained:

$$ft_{1/2} = \frac{\ln(2)h^7}{64\pi^4 g^2 m_e^5 c^4 \left| M_{if} \right|^2}. \tag{2.7}$$

Left hand side of the equation is called a comparative half-life, which provides a basis for the classification of the beta transitions. Equation also implies that the differences in the ft-values are related to the matrix elements, which are obtained from the nuclear model calculations. Expression of the beta decay matrix element will be referred in the context of different

7

approaches. Due to the wide range of the *ft*-values, their logarithms are used instead. Classification of the beta-transition according to their log *ft* values is presented in Table 2.2.

Table 2.2   Typical log *ft* values of different types of beta decay transitions.

Transition type	ΔI	Δπ	Log *ft*
Super allowed (ΔT=0)	0	no	3.48-3.50
Allowed	0,1	no (Δ*l*=0)	< 5.9
Allowed, 1-forbidden (ΔI≥2)	0,1	no (Δ*l*=2)	> 6
First forbidden	0,1	yes	7(1)
First forbidden unique	2	yes	8.5(5)
Second forbidden	2,3	no	≈13
Third forbidden	3,4	yes	≈18

2.1.4   Shell model of the nucleus

The systematics of the neutron and the proton separation energies and the systematics of the energy of the first 2^+ state, among many other observables, reveal existence of the magic numbers and shell structure of the nucleus. The shell model was adopted from the atomic physics where its success has been unquestionable. In the case of atomic physics, electrons are moving in the central field generated by the point like charge of the nucleus. In the nucleus itself there is no additional source of potential, but the nucleons are moving in the central field generated by the interactions between nucleons. Despite of this basic difference, the shell model has been very successful also in nuclear physics.

Appearance of the magic numbers requires the use of the potential which can reproduce the observed energy gaps. A central field has often been introduced as an isotropic harmonic oscillator (HO) potential due to its mathematical simplicity. A radial dependence of the potential can be written as

$$V(r) = \tfrac{1}{2} M\omega^2 r^2, \tag{2.8}$$

where M is a mass of the nucleon, $\hbar\omega$ is an energy quantum of the harmonic oscillator and r is a distance between a nucleon and the origin of the coordinate frame. The Schrödinger equation of the nucleon in the HO-potential,

$$\left(\frac{p^2}{2M} + \tfrac{1}{2} M\omega^2 r \right) \phi(r) = E\phi(r), \tag{2.9}$$

can be solved analytically resulting in the eigenstates of the harmonic oscillator $E_{nl} = (2n + l - \frac{1}{2})\hbar\omega$, which are equally spaced and degenerate corresponding to different orbital angular momentum l values.

Inclusion of a phenomenological l^2-dependent term leads to the so called modified harmonic oscillator, which is flattered at the bottom of the potential. Due to that, energy levels with high l-value are lowered in energy as compared to the degenerate levels. However, this is not enough to reproduce all of the observed magic numbers. Only the inclusion of an attractive spin-orbit interaction reproduces the experimentally observed magic numbers 2, 20, 28, 50, 82, and 126. This interaction lowers the states with a total angular momentum $j=l+1/2$ and raises the states with $j=l-1/2$. The magnitude of the splitting depends on the l-value and the mass A of the nucleus. Experimentally observed splitting of the states with $j=l\pm1/2$ is written approximately [Sol76]

$$\Delta E_{ls} \approx -20l \cdot sA^{2/3} \, \mathrm{MeV}. \tag{2.10}$$

The resulting eigenstates are characterized by n, l, and j quantum numbers, which are conserved in the spherical potential.

A more realistic radial dependence of the nuclear potential is given by the Woods-Saxon potential. Its radial dependence follows the nuclear matter distribution with almost constant depth. In sect. 2.1.7 the Woods-Saxon potential is applied in the calculation of the single-particle levels in deformed potential.

2.1.5 Collective properties of the nucleus

Although the shell model can reproduce many properties of light nuclei, it has not been used very much in medium and heavy nuclei. This is related to the computational difficulties of the model when applied in multi-j configurations, which lead to the extremely large matrices.

Two approaches have been used among the heavy nuclei. A collective model of Bohr and Mottelson [Boh75] is concentrated on macroscopic motions and excitations of a nucleus. Another approach follows the idea of the shell model, but uses potential having deformed shape. The latter one is known also as the Nilsson model [Nil55]. Both the collective model and the Nilsson model include the non spherical shape of the nucleus.

The shape of the nucleus is often taken as a an ellipsoid of revolution. In the simplest case, the shape is distorted in one direction either by elongating or compressing it. The first case corresponds to a *prolate* (American football like) deformation and the latter one is called *oblate* (disc like) deformation. Both of these are examples of the axially symmetric shapes. A commonly used presentation for the shape of the nucleus is the so called β_l parametrization, where the l denotes the multipole of the spherical harmonics. Inclusion of the higher orders

than 2, which corresponds to the already discussed quadrupole distortion, results in more complicated shapes, but the axial symmetry remains.

The axially asymmetric shapes are also possible. The so called $\beta\gamma$-parametrization of the shape of the nucleus includes also axially asymmetric shapes. The shape of the nucleus is presented with two parameters, quadrupole distortion β and axially asymmetry parameter γ. In the convention used in [Cha91] prolate and oblate shapes correspond to $\beta>0$ and γ-deformation either $\gamma=0°$ or $\gamma=60°$, respectively. In the case of the non-zero β-deformation and the γ-deformation other than $0°$ or $60°$, the shape of the nucleus in non-axial. In the model of Davydov *et al.* [Dav58] the nucleus has a stable axially asymmetric shape. Another extreme, the total instability in the γ-direction, corresponds to a γ-vibration of the nucleus having the quadrupole deformation β. The former model is called Davydov model and the latter one is the Wilets-Jean model [Wil56]. Among the experimental data, there is no evidence for the rigid triaxiality, but rather triaxiality is associated with γ-softness [Cas90].

2.1.6 Deformed shell model

In the shell model picture the spherical shape of the potential was assumed. As a result of the obvious need for the non-spherical shape, the shell model was improved by Nilsson [Nil55] by describing the motion of particles in a potential with non-spherical shape. The potential had the form of an anisotropic harmonic potential, which also contained the l^2-dependent term and spin-orbit coupling. Due to the deformation the $(2j+1)/2$-fold degeneracy of the shell model states is broken over $|m|$-values. Resulting state is still doubly generate corresponding to $\pm m$-values. A total angular momentum j is no longer good quantum number, but the states are characterized by their energy, parity and projection K of the total angular momentum against the nuclear symmetry axis. However, K an π do not fully characterize the resulting states. The asymptotic quantum numbers are needed to complement them. In the original paper of Nilsson, the states were labeled by the quantum numbers [$Nl\Lambda\Sigma$] corresponding to the spherical harmonic oscillator basis, but the [$Nn_z\Lambda\Sigma$] presentation corresponding to cylindrical harmonic oscillator basis, is also used.

In this thesis the single particle levels in the deformed potential are calculated using the computer code *WSBETA* reported in [Cwi89]. It is based on the axially deformed Woods-Saxon potential reported in Ref. [Dud79]. For the axial shapes, the nuclear surface can be written as

$$R\left(\cos\theta,\tilde{\beta}\right) = c\left(\tilde{\beta}\right)R_0\left[1 + \sum_{\lambda\geq 2}\beta_\lambda Y_{\lambda 0}(\cos\theta)\right] \tag{2.11}$$

where $Y_{\lambda m}(\cos\theta)$ are the spherical harmonics. A deformed Woods-Saxon potential is defined as

$$V\left(\mathbf{r},\tilde{\beta}\right) = \frac{V_0}{1+\exp\left[dist_\Sigma\left(\mathbf{r},\tilde{\beta}\right)/a\right]} \tag{2.12}$$

where $dist_\Sigma\left(\mathbf{r},\tilde{\beta}\right)$ equals to the distance between the point r and the nuclear surface represented by equation (2.11). Depth of the potential is given by the V_0 and a is a surface diffuseness.

The spin-orbit potential is written as

$$V\left(\mathbf{r},\tilde{\beta}\right) = \lambda\left(\frac{\hbar}{2Mc}\right)^2 \left\{\nabla\frac{V_0}{1+\exp\left[dist_{\Sigma_{so}}\left(\mathbf{r},\tilde{\beta}\right)/a\right]}\right\}(\mathbf{r}\times\mathbf{p}), \tag{2.13}$$

where λ is a strength of the spin-orbit potential, σ is a vector operator composed of Pauli matrices and $\mathbf{p}$ is a linear momentum operator. The Coulomb potential for protons corresponds to the uniformly distributed nuclear charge equal to $(Z-1)e$ inside the nuclear surface Σ. It is computed by using the expression given in Ref. [Hil53].

The depth V_0 for the central potential and spin-orbit-potential is parametrized as

$$V_0 = \tilde{V}\left(1\pm\kappa\frac{N-Z}{N+Z}\right) \quad,\text{where} \quad \begin{cases} + & \text{for protons} \\ - & \text{for neutrons} \end{cases} \tag{2.14}$$

The single-particle energies and the wave functions are calculated by using the harmonic oscillator basis. Hamiltonian including central, spin-orbit and Coulomb potentials was diagonalized in the axially deformed harmonic oscillator basis and then the deformed WS-potential was generated numerically at a deformation specified. The details of the solving the Hamiltonian are presented in [Cwi87]. The calculated single-particle states in the vicinity of [110]Ru (66 neutrons and 44 protons) are presented in Figs. 2.1 and 2.2 The asymptotic quantum numbers in cylindrical basis $\Omega^\pi[Nn_z\Lambda]$ are presented in the right side of the figures. Spherical shell model states are also labeled.

Parameters of the central potential are equal to those given in Ref. [Ros68]. More important than the parameters of the central potential, is the choice of the parameters for the spin-orbit potential. In this work, a "universal set" of parameters given in Ref. [Cwi87] was applied. This set has its basis on the high spin studies in the [208]Pb-region [Dud81] and in the [148]Gd nucleus [Dud82]. This set is appropriate for the transitional region below Z=50. According to the extensive study of different parametrization in Ref. [Pen92], use of the other values do not improve the results in the region of interest. This set has been applied also in Refs. [Ryk89,Möl90,Vir90]. The values of the universal parameters are collected in Table 2.3.

Table 2.3   "Universal" parameter set for Woods-Saxon potential.

Parameter	N	P
Depth of the central potential $\tilde{V}$ [MeV]	49.6	49.6
Radius parameter of the central potential r_0 [fm]	1.347	1.275
Diffuseness parameter of the central potential a [fm]	0.7	0.7
Strength of the spin-orbit potential λ	35.0	36.0
Radius parameter of the spin-orbit potential r_{so} [fm]	1.310	1.20
Diffuseness parameter of the spin-orbit potential a_{so} [fm]	0.7	0.7
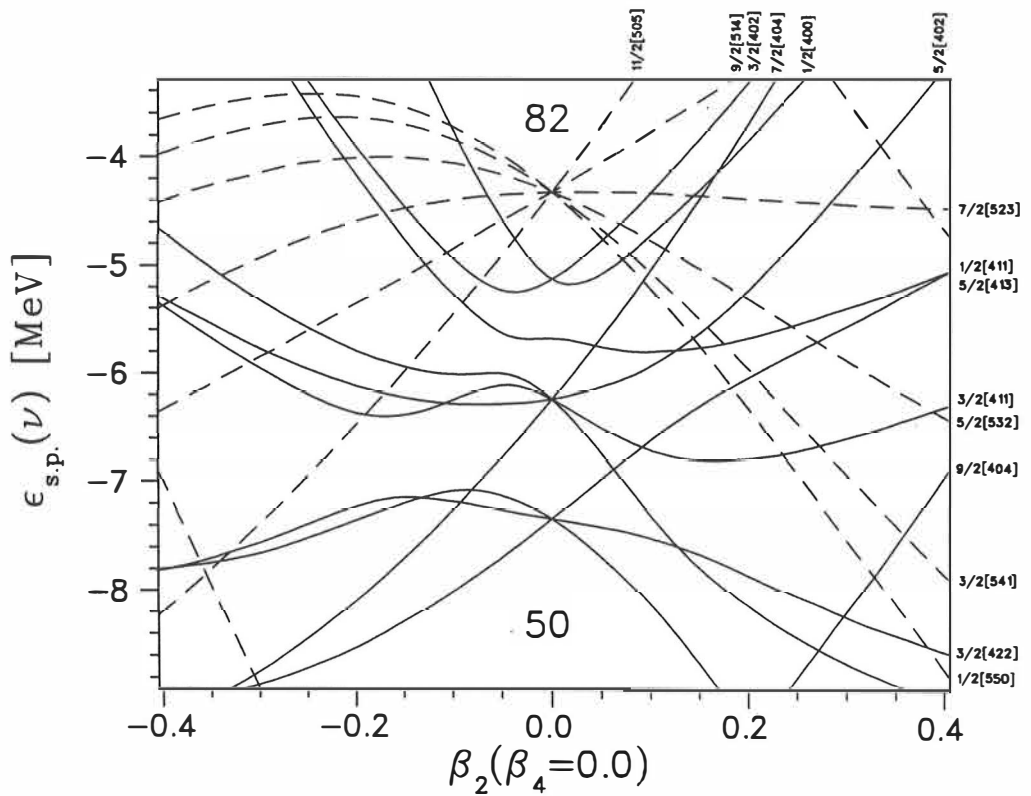
Figure 2.1   Neutron single-particle states in the deformed shell model around N=66.
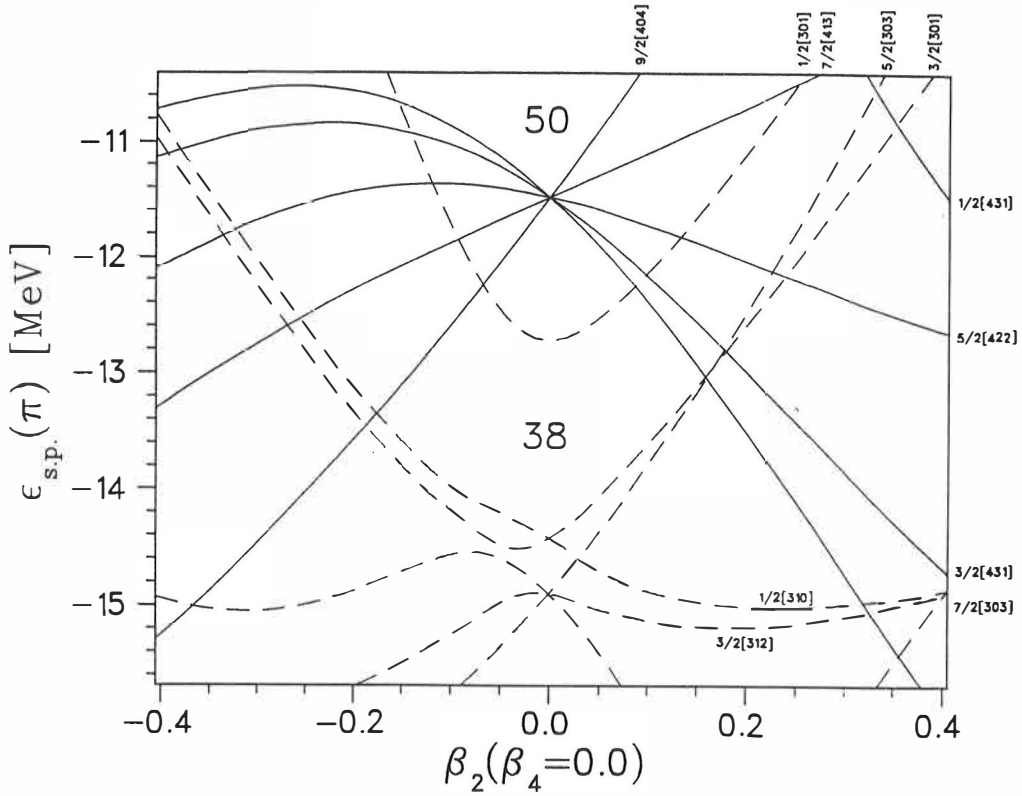
Figure 2.2   Proton single-particle states in the deformed shell model around Z=44.

2.1.7   Beta decay matrix elements

Extreme single particle shell model.

In a single particle model, an inert core with J=T=0 and a single valence nucleon outside the core is assumed. Thus a beta decay involves the transformation of one nucleon from the $l_i j_i$ initial state to the $l_f j_f$ final state. The simple expression for the matrix element of allowed beta decay in that case is obtained,

$$\left\langle M_{GT}\right\rangle^2_{s.p.} = 6\left(2 j_f +1\right)\begin{Bmatrix} \frac{1}{2} & \frac{1}{2} & 1 \\ j_i & j_f & l \end{Bmatrix}^2 \tag{2.15}$$

which reduces to the equation

$$\left\langle M_{GT}\right\rangle^2_{s.p.} = \frac{2 j_f +1}{j_f} \tag{2.16}$$

in the case of β^- decay from $j_i = l - \frac{1}{2}$ state to $j_f = l + \frac{1}{2}$ state [Bru77].

Deformed shell model

In the deformed case, the intrinsic matrix element of beta decay can be written as

$$\langle M_{GT} \rangle^2_{s.p.} = 2\left[\sum_l a^K_{l,\Lambda,\Sigma=-\frac{1}{2}} a^{K+1}_{l,\Lambda,\Sigma=-\frac{1}{2}} \right]^2 \tag{2.17}$$

with K being the smaller of K_i and K_f. Amplitudes $a^K_{l,\Lambda,\Sigma}$ are taken from the nuclear model calculations. In the asymptotic limit only one wave function component dominates with $a^K_{l,\Lambda,\Sigma}$ close to unity. As a consequence, the value of the matrix element approaches to 2 [Boh75].

2.2 Macroscopic-microscopic model

As the other macroscopic-microscopic models the total energy of the nucleus is calculated by summing the contributions from the macroscopic and microscopic parts:

$$E_{tot}(\beta) = E_{mac}(\beta) + E_{mic}(\beta) \tag{2.18}$$

A shape of the nucleus is obtained by minimizing E_{tot} in an appropriate deformation space denoted by β in the equation above. The deformation space of the present version of the model is limited to the axially symmetric shapes. The microscopic part in the equation (2.18) includes the shell correction and pairing terms. The shell correction is based on the Woods-Saxon potential described in the previous chapter.

2.2.1 Liquid drop mass equation

The macroscopic part of the model is taken either from the liquid drop model of Myers and Swiatecki [Mye66] or from the Yukawa-plus-exponential mass formula of Möller and Nix [Möl81]. In this work the former one has been used. The macroscopic energy of the nucleus with Z protons and N neutrons is written

$$B_{LD} = 17.9439 A^{2/3} T - 15.4941 AT + 0.7053 \frac{Z^2}{A^{1/3}} - 1.152596 \frac{Z^2}{A} \tag{2.19.a}$$

where

$$T = 1.0 - 1.7826 \left(\frac{N-Z}{A} \right)^2 \tag{2.19.b}$$

is an isovector term. The liquid drop model has been the most extensively used approach for the parametrization of the bulk energy of the nucleus. After its invention various refinements have been added to it but it is still widely used in the original form, too.

14

2.2.2 Pairing corrections

The pairing was treated in the Lipkin-Nogami extension [Lip60,Nog64,Pra73] of the BCS-approximation [Ogl71]. The pairing gap Δ and Fermi energy λ and the occupation probabilities v_k^2 are obtained by solving the coupled nonlinear equations

$$N_{tot} = 2\sum_{k=n}^{m} v_k^2 + 2(n-1) \tag{2.20}$$

$$\frac{2}{G} = \sum_{k=n}^{m} \frac{1}{\sqrt{\tilde{\varepsilon}_k^2 + \Delta^2}} \tag{2.21}$$

$$v_k^2 = \frac{1}{2}\left(1 - \frac{\tilde{\varepsilon}_k}{\sqrt{\tilde{\varepsilon}_k^2 + \Delta^2}}\right) \qquad ,k = n, n+1,\ldots,m \tag{2.22}$$

with a definition

$$\tilde{\varepsilon}_k = \varepsilon_k - \lambda. \tag{2.23}$$

ε_k denotes the shifted single particle energies according to the equation

$$\varepsilon_k = \varepsilon_{s.p.} + (4\lambda_2 - G)v_k^2 \qquad ,k = n, n+1,\ldots,m \tag{2.24}$$

where λ_2 is a number fluctuation constant. The pairing strengths G for neutrons and protons are obtained from the average pairing gap energies of A.S. Jensen et al. [Jen84], which were multiplied by 0.9 as suggested by K. Rykaczewski [Ryk90].

2.3 Theoretical calculations within the macroscopic-microscopic model

In the study of the decay of Pd-isotopes, the QRPA-model of J. Suhonen et al. was applied [Suh92,Suh88]. Use of this model in the case of Ru-isotopes showed that the spherical approach could not reproduce the decay properties of these isotopes. However, the macroscopic-microscopic model [Cwi87], which was presented in section 2.2, could reproduce the experimental decay energies of $^{108-114}$Ru and the distribution of Gamow-Teller strength [Jok91,Jok92,Jok93] in $^{108-112}$Rh isotopes. This model was also applied in the study of Pd-isotopes [Kop89,Jan93], in the decay of ^{106,108}Mo-isotopes[Jok94] and in neutron-deficient Sn-isotopes [Dob88].

2.3.1 Even-even parent nucleus

The ground state shape of the beta-decaying parent nucleus was obtained from the energy minimum of the potential energy surface in two-dimensional deformation space (β_2, β_4). In each (β_2, β_4)-point of the (β_2, β_4)-grid the potential energy of the nucleus was calculated by using the single-particle spectrum generated at the corresponding deformation including

pairing. These were combined with the macroscopic part by using Strutinsky's shell correction method [Str67,Str68]. The (β_2,β_4)-grid of the calculations were chosen in a following way:

$$\beta_2 = -0.4,(0.04),+0.4 \quad \beta_4 = -0.1,(0.02),+0.1, \quad \text{Cd, Pd, and Ru isotopes}$$
$$\beta_2 = -0.48,(0.04),+0.48 \quad \beta_4 = -0.1,(0.02),+0.1 \quad \text{Mo, and Zr isotopes}$$

Figure 2.3. presents the contour maps of the potential energy surfaces of the ground states of $^{118\text{-}124}$Cd, $^{112\text{-}120}$Pd, $^{106\text{-}114}$Ru, $^{102\text{-}110}$Mo, $^{100\text{-}104}$Zr and $^{98\text{-}102}$Sr isotopes.
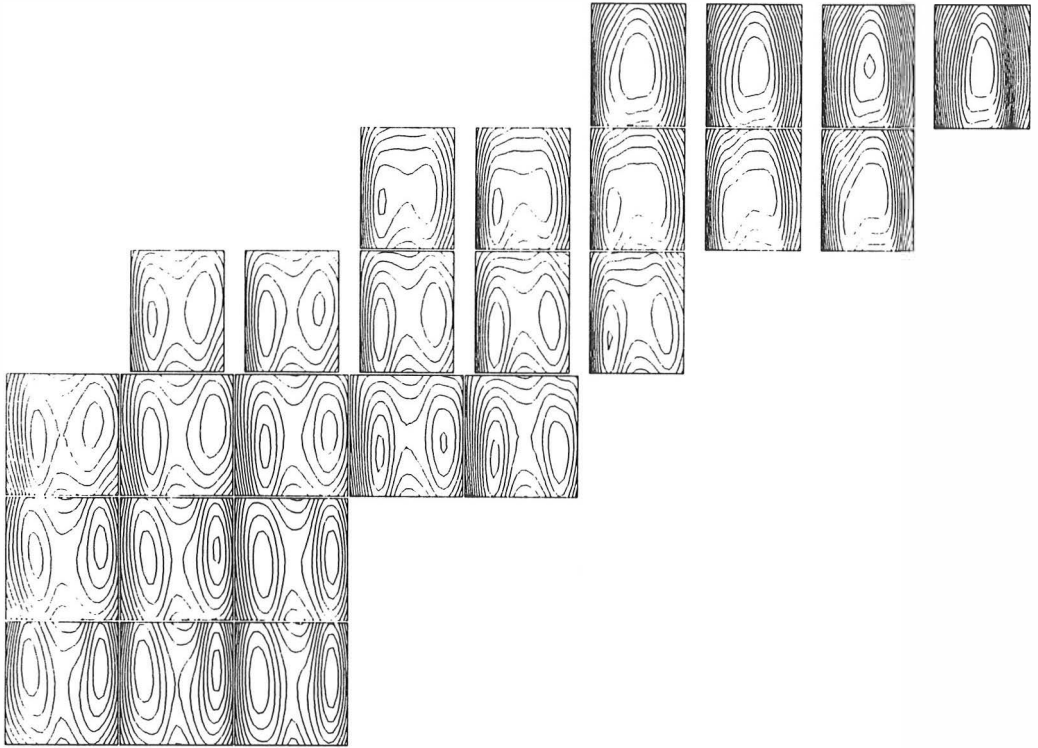
Figure 2.3   Contour maps of the ground state energies of even-A Cd, Pd, Ru, Mo, Zr and Sr-isotopes. Maps of the isotopes are organized as isotopes appear in the chart of nuclides. The β_2-deformation is presented in horizontal axis from -0.48 to +0.48 and vertical axis corresponds to β_4 deformation in the range from -0.1 to +0.1. Separation of the contour levels is 750 keV.

According to [Sol76] deformation energy $E_{def}(\beta)$ is defined as a difference between the potential energy in spherical shape and the energy minimum at deformation β. The obtained deformation energies for Pd, Ru and Mo are listed in Table 2.4. It includes also the energy difference of the oblate and prolate minima if both exist. The occupation factors u^2 and v^2 of the single particle levels in the ground state minimum were extracted by using the Lipkin-

Nogami extension for the BCS-method. These were later used for the pairing correction in the calculation of the Gamow-Teller strength of each $0^+ \rightarrow 1^+$ transition.

Table 2.4 The quadrupole deformations and deformation energies of Pd, Ru, and Mo isotopes. Both oblate and prolate minima are included. The deformation energies are given in MeV units.

	β_2	$E_{def}(\beta)$	β_2	$E_{def}(\beta)$
^{112}Pd	-0.22	0.80	+0.16	0.45
^{114}Pd	-0.22	0.90	+0.18	0.36
^{116}Pd	-0.22	0.72	+0.16	0.22
^{118}Pd	-0.19	0.26	+0.11	0.06
^{120}Pd	-0.01	0.08	+0.08	0.004
^{106}Ru	-0.22	1.22	+0.21	0.93
^{108}Ru	-0.22	1.58	+0.24	1.04
^{110}Ru	-0.23	1.91	+0.24	1.14
^{112}Ru	-0.23	2.04	+0.24	1.10
^{114}Ru	-0.23	1.87	+0.23	0.88
^{102}Mo	-0.20	1.26	+0.27	1.08
^{104}Mo	-0.22	1.72	+0.32	1.74
^{106}Mo	-0.22	2.11	+0.32	2.12
^{108}Mo	-0.23	2.45	+0.32	2.29
^{110}Mo	-0.23	2.58	+0.31	2.27

2.3.2 Two-quasi particle spectrum of the odd-odd daughter nucleus

Two quasi-particle spectra of the odd-odd daughter nuclei were calculated by summing the obtained quasi-particle energies of neutrons and protons. Altogether 16 neutron states originating from the shell model states $d_{5/2}$, $g_{7/2}$, $s_{1/2}$, $d_{3/2}$, and $h_{11/2}$ and 14 proton states originating from the $f_{5/2}$, $p_{3/2}$, $p_{1/2}$, $g_{9/2}$, and $d_{5/2}$ shell model states were included in calculations. No residual pn-interaction was included, but pairing of the like-nucleons was taken into account. The energy of each neutron-proton two quasi particle-state was minimized in (β_2, β_4)-grid. Thus, the resulting spectrum of excited states contains states with various deformations. The individual quasi particle-energies, in turn, were calculated using the equation

$$\varepsilon_{q.p.} = \sqrt{\tilde{\varepsilon}_k^2 + \Delta^2} + \lambda_2, \qquad k = n, n+1, \ldots, m \tag{2.25}$$

Due to the selection rules of the beta decay, only 1^+ states are populated by the allowed decay of the 0^+ initial state of an even-even parent nucleus. Thus, the main emphasis has been put on the 2-quasi particle final states with spin and parity equal to 1^+. The calculated 1^+ final states are presented later in Figs 5.11 and 5.12, where they are compared to the observed level scheme.

2.3.3 Decay energies and half-lives in the macroscopic-microscopic model

The decay energies were calculated as the difference of the ground state energies of the even-even parent nucleus and the odd-odd daughter nucleus. They are presented in Table 2.5. In addition, the GT-strengths connected to each $0^+ \rightarrow 1^+$ beta transition were calculated according to the equation

$$B_{GT} = \gamma^2 \left\langle I_i K_i 1 (K_f - K_i) \middle| I_f K_f \right\rangle^2 R^2 \times \begin{cases} 2, & \text{if } 0^\pm \rightarrow 1^\pm \\ 1, & \text{otherwise} \end{cases} \tag{2.26}$$

where $\gamma^2 =$ is an intrinsic matrix element between initial and final state as presented in Eq. (2.17). $R^2 = u_\pi^2 v_\upsilon^2$ is a pairing factor, which takes into account the emptiness and fullness of the final and initial states, respectively. Clebsch-Gordan coefficient and the multiplication factor constitutes the statistical factor accounting for the summation over the final spin states and averaging over the initial spin states in deformed nuclei [Sol76].

A total beta half-life was then calculated according to the equation

$$T_{1/2}(\beta^-) = \left[\sum_{i=0}^{E_i < Q} \frac{1}{t_{1/2}(i)} \right]^{-1} \tag{2.27}$$

where $t_{1/2}$ is a partial half-life of the beta transition to a two-quasi particle final state at excitation energy E_i. Due to the existence of the two competing shapes, the half-lives were estimated both for the oblate and prolate cases. Also the total GT-strength was calculated separately for the oblate and prolate deformations. Additionally, the calculated excited spectra were used to estimate the average energy of 1^+ states inside the decay energy window. The weighting factor for averaging was taken from the calculated GT-strength of each transition.

Table 2.5 Calculated beta decay properties of even-A Pd, Ru and Mo-isotopes.

	Q_β [MeV]	Oblate deformation			Prolate deformation		
		$T_{1/2}$ [s]	B(GT)	$\log ft$	$T_{1/2}$ [s]	B(GT)	$\log ft$
^{112}Pd	0.9	3600	0.35	4.05	586	1.01	3.58
^{114}Pd	2.13	54.6	2.35	3.22	21.2	1.58	3.39
^{116}Pd	3.50	6.88	4.74	2.91	2.04	2.22	3.24
^{118}Pd	4.94	2.57	4.56	2.93	0.26	2.63	3.17
^{120}Pd	6.21	0.44	2.87	3.13	0.25	1.14	3.53
^{106}Ru	0.68	5460	0.66	3.77	3060	0.36	4.03
^{108}Ru	2.03	21.1	0.93	3.62	48.0	0.71	3.74
^{110}Ru	3.44	1.71	3.35	3.06	3.60	1.45	3.42
^{112}Ru	4.75	0.48	5.34	2.86	0.62	2.23	3.24
^{114}Ru	6.27	0.14	5.93	2.81	0.16	2.80	3.14
^{102}Mo	1.36	207	1.22	3.50	14410	0.08	4.69
^{104}Mo	2.80	5.72	1.14	3.53	79.6	0.30	4.10
^{106}Mo	4.24	0.6	3.56	3.03	2.88	0.67	3.76
^{108}Mo	5.64	0.12	4.47	2.94	0.29	1.24	3.49
^{110}Mo	7.25	0.052	6.38	2.78	0.064	2.38	3.21

2.4 Atomic mass calculations

A great effort has been put on the development of models, which can predict the binding energies of nuclei. The latest compilation from 1988 edited by P. Haustein [Hau88] contains eight different atomic mass predictions and since then at least three new sets of atomic mass predictions have been reported. In the following the mass predictions are divided into four separate classes, which are

1) Mass relations. They are based on the simple symmetrical relationship between the unknown and the neighboring nuclei.

2) Mass equations. This category includes models, which use the simple phenomenological approach to parametrize the known mass surface and local irregularities of mass surface.

3) Macroscopic-microscopic models. In these models the main part of the total energy is calculated in the macroscopic model, which is often liquid drop model (LD) or droplet model (DM) or their revised versions with finite range. Local irregularities of the mass surface are treated in microscopic corrections, which include both the shell structure and the pairing correlations.

4) Self-consistent calculations. These are purely microscopic approaches. Due to the computational limitations, especially in deformed nuclei, Hartree Fock calculation are normally limited for the small mass region.

A common feature for all models is that mathematical expression of the mass surface is parametrized in known mass surface and then the atomic masses are predicted up to the drip-line and even beyond that. The predictive power of the models varies greatly. Some of the models can reproduce the known mass surface with high accuracy but predictions do not agree with new experimental results. This is often related to the large number of parameters, which result in a good reproduction of input values, but may lead to diverging predictions in the new regions. Additionally, one should bear in mind that often more important than the absolute value is the overall trend of the mass surface. This can also tell how well the model can predict atomic masses beyond the known mass surface.

Table 2.6   Summary of the atomic mass predictions mentioned in 1988 atomic mass compilation edited by P. Haustein [Hau88]. Three new set of atomic mass prediction are also included in the table.

Abbr.	Year	# of par.	RMS-dev.	Short description of the model	Ref.
PA	1988		271	Mass relation based on the isobaric mass equation	Pap88
DCZ	1988	45	287	Phenomenological model based on the α-line systematics	Dus88
MN	1988	26	849	Macroscopic-microscopic model	Möl88
MMST	1988	29	777	Macroscopic-microscopic model	Möl88
CKZ	1988		431	Mass relation based on the Garvey-Kelson relation	Com88
SN	1988	238	456	Mass equation based on the infinite nuclear matter with local corrections	Sat88
TMYY	1988	281	538	Empirical mass formula with proton-neutron interaction	Tac88
SJ	1988	12	512	Modified Bethe-Weizsäcker mass formula with deformation and shell correction	Spa88
JM	1988	928	343	Mass relation based on the Garvey-Kelson relation	Jän88
MJ	1988	471	346	Mass relation based on the Garvey-Kelson relation	Mas88
W88	1988			Combination of the experimental data and extrapolations	Wap88
P92	1992	9	730	Hartree-Fock method	Abu92
M93	1993	37	669	Macroscopic-microscopic model	Möl93
AW	1993			Combination of the experimental data and extrapolation	Aud93

Table 2.6 summarizes the main characters of the 1988 and the latest atomic mass predictions. The list of table is not complete nor it can be, but it represents a set of atomic mass predictions, which are widely used and referenced in the physics literature. In the following chapters the experimental results are compared to the representatives of each category of atomic mass predictions. Main emphasis have been put on the systematic behavior of the different models far from the stability. The atomic mass predictions chosen for the comparison are presented below.

Mass relation of J. Jänecke and P. Masson

In the model of Jänecke and Masson, the atomic masses of nuclei with $N>Z$ are predicted by using the transverse Garvey-Kelson relation [Gar66,Gar69]. According to the relation the equation

$$
\begin{aligned}
& M(N+2,Z-2)-M(N,Z)+M(N+1,Z)- \\
& M(N+2,Z-1)+M(N,Z-1)-M(N+1,Z-2) \approx 0
\end{aligned}
\tag{2.26}
$$

is the simplest non-trivial homogeneous mass relation. This relation cancels the role of the effective pp-, nn- and pn-interactions and single-particle energies assuming that these quantities vary slowly with mass number A. If this relation is presented in a homogeneous third-order partial differential equation, one obtains the general solution

$$
M(N,Z) = G_1(N) + G_2(Z) + G_3(A)
\tag{2.27}
$$

The mass parameters $G_1(N)$, $G_2(Z)$ and $G_3(A)$ are arbitrary point functions of their arguments and they can be constructed uniquely by minimizing the difference $M(N,Z)-M_{exp}(N,Z)$ [Jän88].

Phenomenological model of T. Tachibana et al.

The atomic mass predictions of T. Tachibana *et al.* [Tac88a] serve as an example of the purely phenomenological approach. It is an improved version of the Uno-Yamada mass equation [Uno81,Uno82]. A ground state mass of a nucleus consisting of Z protons and N neutrons can be expressed with three terms:

$$
M(Z,N) = M_g(Z,N) + M_{eo}(Z,N) + M_s(Z,N)
\tag{2.28}
$$

The first term is a smooth function of N and Z, which describes the general feature of the mass surface. It is quite similar to the conventional liquid drop formula, although there are few differences. The second term, M_{eo} takes into account the odd-even effect and the third term includes the deformation and shell structure. The third term is a purely phenomenological one, which is formulated to take into account the mutual support of nuclear magicities and co-operative deformation effect [Tac88a].

Macroscopic-microscopic model of P. Möller et al.

This model has its roots in a study of fission phenomena and especially in the study of the shape of the fission barrier. In the model, the collective behavior of the nuclei is combined with shell structure. The total potential energy of the nucleus with Z protons, N neutron and generic shape S is a sum of the macroscopic term corresponding to spherical shape and the microscopic term

$$E_{pot}(N,Z,S) = E_{mac}(N,Z,S) + E_{mic}(N,Z,S) \qquad (2.29)$$

In their latest set of ground state masses, Möller *et al.* include two different models for the macroscopic part, namely the finite range droplet model (FRDM) and finite range liquid drop model (FRLDM), of which they prefer the former one. The latter one was used in their atomic mass prediction in 1981 [Möl81]. The former one was reported in their midstream atomic mass evaluation in 1988 [Möl88], which included many unresolved questions solved in Ref. [Möl93].

In addition to collective properties, the non uniform distribution of the single particle levels requires the microscopic treatment. The microscopic part is a sum of the shell correction and pairing terms

$$E_{mic}(N,Z,S) = E_{shell}(N,Z,S) + E_{pair}(N,Z,S) \qquad (2.30)$$

These terms can be taken from the single particle states calculated in deformed potential of the folded-Yukawa type [Bol72]. The calculation of shell correction is based on the Strutinsky method [Str67,Str68], which allows the calculation of the nuclear potential energy for the arbitrary shape of the nucleus. The pairing term is calculated with the Lipkin-Nogami approximation [Pra73] for BCS-theory. The macroscopic-microscopic model of P. Möller *et al.* provides a state-of-art-model of the DM-based models and is often referenced, when other approaches are compared to DM-models.

Hartree-Fock method of J.M. Pearson et al.

This approach, of which the latest version is reported in [Abu92] and which is developed in Refs. [Dut86,Ton87,Pea91], has a completely microscopic background. It is based on the Hartree-Fock method for a Skyrme-type force with a Strutinsky integral (SI) shell correction. The enormous computing time needed for the Hartree-Fock calculation is reduced by using a semi-classical approach, the so called extended Thomas-Fermi (ETF) approximation. Underlying Skyrme-forces and δ-function require only 9 parameters, which are fitted to 1492 masses above A=36. Rms-deviation among the known masses is 0.73 MeV, which is comparable to the best DM-based mass formulae.

Atomic mass extrapolation of G. Audi et al.

The atomic mass tables of H. Wapstra and G. Audi have provided a widely used standard for atomic masses since "The 1971 Atomic Mass Evaluation" by A.H. Wapstra and N.B. Gove. The atomic masses are mainly based on the experimental data, but in the case of clear disagreement between an experimental result and smooth behavior of the mass surface the experimental value is replaced with the rounded value. Smoothing of the mass surface relies on the variety of systematic diagrams. These diagrams include the separation energy of two neutrons (S_{2n}) or two protons (S_{2p}), the decay energy of double beta decay ($Q_{\beta\beta}$) and decay energy of alpha decay (Q_α). A common feature is that they cancel the pairing effect.

2.5 Half-life calculations

Half-life predictions of the various decay modes play an important role in the explanation of the synthesis of the elements in the universe. Various theories have been developed to predict the decay rates of nuclei far from stability. In the following the summary of the most common β-decay rate predictions are given.

2.5.1 Gross theory of beta decay

The first version of the gross theory was formulated by Takahashi, Yamada and Koyama and their first half-life predictions were reported in [Tak73]. This model is based on the averaging of the beta strength distribution in the daughter nucleus. It does not include shell effects except via the mass predictions. However, it takes into account both the allowed and first-forbidden transitions. In the early version of the gross theory, the atomic masses were taken from the mass theory of Myers and Swiatecki [Mye66]. In the model, the strength function for beta-transitions of the type-Ω is given as

$$\left|M_\Omega(E)\right|^2 = \int_{\varepsilon_{min}}^{\varepsilon_{max}} D_\Omega(E,\varepsilon)W(E,\varepsilon)\frac{dn_1}{d\varepsilon}d\varepsilon \qquad (2.31)$$

where E is the energy of the final nuclear and ε is the nuclear single-particle energy state, $dn_1/d\varepsilon$ is the single-particle level density according to Fermi gas model and $D_\Omega(E,\varepsilon)$ is the single-particle strength function. $W(E,\varepsilon)$ is the weight function, which takes into account the Pauli principle.

Tachibana *et al.* have reported improvement for the gross theory of beta decay [Tac88], which was used to calculate new half-life predictions. Their improvements include the better treatment of pairing, which takes into account the retardation of the beta transition from the unpaired nucleon (odd-A or odd-odd cases). The second improvement modifies the cut-off energy of the single-particle strength function so that the non-energy-weighted sum rule for the Fermi transitions is better fulfilled. The third improvement concerns single-particle strength

function itself, which has been modified to reproduce the observed shape of the strength function.

2.5.2 TDA-approach of H.V. Klapdor *et al.*

This model is based on the microscopic theory and it provides a more realistic description of the beta strength function as compared to previous model. In the model Tamm-Dancoff approximation is solved analytically by the use of the schematic model for a long-range Gamow-Teller residual interaction. It can take into account the collective effects like the observed hindrance of the GT-transitions and the existence of the GT giant resonance (GTGR). Due to formulation of the GT-strength between the initial and the final states, this model is totally independent of the mass predictions and their uncertainties. It also takes into account deformation, although approximately, by calculating the wave functions in a deformed harmonic oscillator potential. The choice of deformation relies on the general systematics. On the contrary to the previous model, it does not include the first forbidden transitions.

2.4.3 QRPA-model of P. Möller and J. Randrup

The most refined models used for the half-life predictions are based on the quasi-particle-random phase approximation (QRPA). In the model of P. Möller *et al.* intrinsic wave functions are constructed by adding to a pure single particle model a pairing interaction and a residual Gamow-Teller-interaction which is treated in the RPA-approximation. Due to the flexibility of the model, various single-particle potentials can be applied. For the calculation of the beta decay rates, a folded-Yukawa (FY) single particle model or Nilsson model has been used as a starting point for the calculation. Pairing is treated in the BCS-procedure with global pairing gap energy of $12\sqrt{A}$. A GT residual interaction is treated in random-phase approximation with a coupling constant $\chi_{GT} = 23/A$ MeV. In the combination with (FY)-potential, a "universal quenching parameter" equal to 2 was applied [Möl90]. However, in our calculations with Nilsson wave functions, this parameter was excluded, as was pointed out in Paper III. The deformation and decay energies are taken from the mass models of Möller and Nix [Möl88], Groote *et al.* [Gro76] or Hilf *et al.* [Hil76]. The present version of the model requires equal deformations of the parent and daughter nucleus and it is restricted to allowed beta transitions.

2.4.4 QRPA-approach of A. Staudt *et al.*

This model has a very similar background as compared to the previous one. The main difference is in the treatment of the GT residual interaction [Sta90]. This model relies on the GT residual interaction coupling constant, which is fitted separately using the known half-lives for each element on the contrary to the global value of P. Möller and J. Randrup. In Ref.

[Sta89] they have tested various mass predictions with the result that the mass model of Möller and Nix [Möl88] should be used when the decay rates are predicted far from the stability. However, among the known decay rates the best agreement is achieved when the mass model of Groote *et al.* [Gro76] is used.

3 Experimental techniques

The neutron-rich nuclei studied in this thesis were produced in a fission reaction and mass separated by using the IGISOL-mass separator at the Department of Physics, University of Jyväskylä. The radioactive decay of the unstable fission products were recorded by using the various γ-, X-, β^- and e^- spectroscopic methods. Details of the experimental methods involved are presented in the following sections.

3.1 Charged particle induced fission

In the study of the neutron-rich medium mass nuclei, fission reaction has been a rich source of new information. The reaction applied has often been either a spontaneous fission or a thermal neutron induced fission. In the former case, the fissioning source is typically one of the Cf-isotopes. In the latter case, ^{235}U has been the most typical fissioning target for thermal neutrons due to very high cross section, even 20 barns for individual fission product [Rav89]. In both cases the fission process is characterized by the low excitation energy. Due to that, the shell effects of the products tend to drive fission into an asymmetric mass division and the higher amounts of nuclei with even Z and/or N are produced than the odd ones. All in all, the low energy fission favors the separation into two different fragments instead of symmetric mass division.

Due to the height and the shape of the fission barrier, the fission of elements below Z=90 results in the symmetric mass distribution of fission products. In the case of a higher Z-number of fissioning nucleus, both asymmetric and symmetric mode of fission can occur in the same time depending on the excitation energy and the shell structure of the fissioning nuclei [Van73]. In the charged-particle induced fission, the excitation of the fissioning compound nucleus is relatively high due to the high energy needed for overcoming the Coulomb barrier between a projectile and a target. As a result of that, the mass distribution is broader and it is peaked in a symmetric mode. The typical mass spectra of the low energy fission and charged particle induced fission are presented in Fig. 3.1.

The charge division in the fission reaction is determined already in scission. The element distribution of fission products in certain mass chains have been studied both in a thermal fission [Wah88] and in a proton induced fission [Lei91,Jau94]. In the neutron induced thermal fission the neutron-to-proton ratio follows the so called ECD hypothesis (Equal Charge Division), where the difference between the most probable charge and the charge of the most stable isobar of a certain mass chain is equal for the light and heavy fragment. On the contrary, in the charged particle induced fission, the charge distribution of the products is found to follow the so called UCD-hypothesis (Unchanged Charge Division), where the neutron-to-

proton ratio of the products is identical to the target nucleus. Additionally, the charge distribution of the latter reaction is broader as compared to the former one. This might be an indication of the higher excitation, which results in a variety of fission channels.
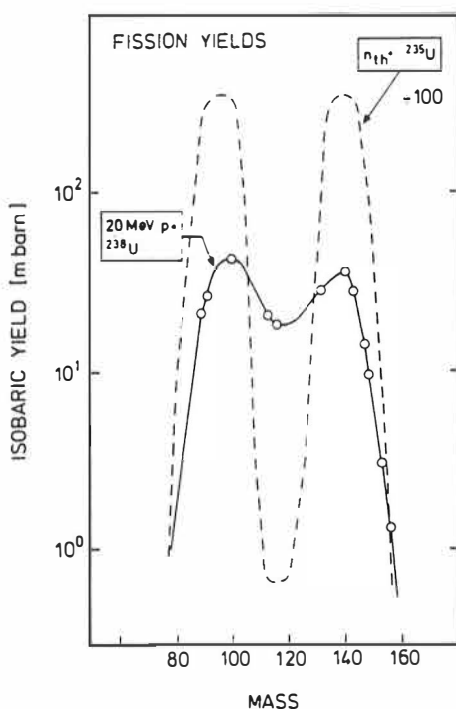
Figure 3.1   A mass distribution of the proton-induced fission and thermal neutron induced fission [Wah88].

Although the fission reaction can typically produce a few hundred different nuclides, the influence of the Q-value of the reaction leads to the production of only a few elements in one isobar. Additionally, the large variation of the half-lives provides the possibility to use pulsing of the experiment to further enhance the production of certain elements as compared to other elements in the same mass chain. Experimentally one of the most important observables is the total production rate. In addition to the mass and charge distribution mentioned above it depends on the total fission cross section. In terms of a total fission cross section, the thermal fission with its cross section exceeding 500 barns is superior as compared to the charged particle-induced fission [Vol89]. Due to the low excitation, neutron evaporation channels are weaker in thermal fission which implies the good production of neutron-rich nuclei. However, a much better peak-to-valley ratio is observed for the proton-induced fission as compared to the thermal fission, and the absolute cross sections in the valley region are comparable for both reactions [Wah88,Bab71,Kar91]. Due to the symmetric division, a projectile and target combination can be better optimized in the charged particle induced fission. An example of the production yields of various elements at the IGISOL facility are illustrated in Fig. 3.2.

27
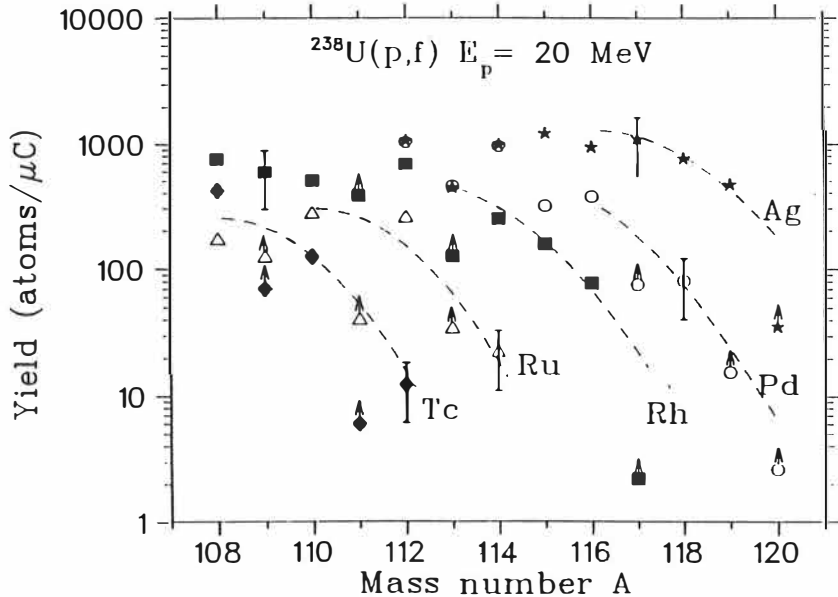
Figure 3.2 Cumulative yields in saturation of Tc, Ru, Rh, Pd and Ag isotopes. Dashed curves are drawn to guide the eye [Lei91].

3.2 Ion Guide Isotope Separator On-Line

3.2.1 Ion guide method

In all experiments a setup of four ^{238}U-targets was used. The thicknesses of the targets were typically 15-20 mg/cm^2 and they were covered with an Al-layer to prevent oxide formation in the uranium. The thickness of the Al-layer was about 0.2 mg/cm^2. The fission targets were situated inside of a small chamber filled with He-gas in about 100 mbar pressure. The transport line of the He-gas was equipped with a LN-cooled trap to decrease the amount of impurities in He-gas, which was standard industrial He-gas with a purity of 99.995 %. The He-pressure and the beam line vacuum were separated with 1.8 mg/cm^2 Havar-foils. The purpose of the He-gas was to slow down the outgoing fission products and also to cool the targets. The interaction between a proton beam and He-gas creates plasma conditions. To avoid this, the fission products were stopped in a plasma-free sub-chamber which was separated from the target volume with the Ni-foil having thickness of 0.9 mg/cm^2. Due to the high first ionization potential of He the fission products attain a 1$^+$ charge state when thermalized. Although the amount of impurities, mainly N_2 (< 10 ppm), H_2 (< 5 ppm) and H_2O (< 10 ppm), is rather low, the oxide formation of a few specific elements was observed as an appearance of activities belonging to A=A-16 mass chain in some experiments. The singly

charged ions were removed from the target chamber by a sonic helium flow through a nozzle with diameter of 0.8-1.5 mm. An evacuation time of the radioactive products from the target chamber was of the order of milliseconds. According to a test measurement referenced in [Tas89], 3.2 ms is needed to remove 50 % of the produced activity out from the target chamber. Figure 3.3 presents the schematic drawing of the target chamber. Outside of the exit hole, the neutral He-gas and charged ions were separated by the combination of an electric field and differential pumping. In the first phase, the bulk of He-gas was pumped by the Roots-pump with a pumping capacity of 4000 m^3/h and the charged ions were directed through the hole in the tip of skimmer electrode by the electric field about -400 V. The distance between the exit hole and the skimmer hole was adjustable from 7 mm to 13 mm. In this section, a typical vacuum was of the order of 0.1 mbar. In the next section of the differential pumping, the ions were first accelerated with 10 kV extraction voltage and the vacuum was improved by using a diffusion pump with the pumping capacity of 2000 l/s. The vacuum inside the second section of differential pumping was about 10^{-4} mbar. In the third section, the ions were accelerated to the final energy of about 40 keV with an acceleration voltage of the order of 40 kV. In this section the vacuum reached the final value of about 10^{-7} mbar.
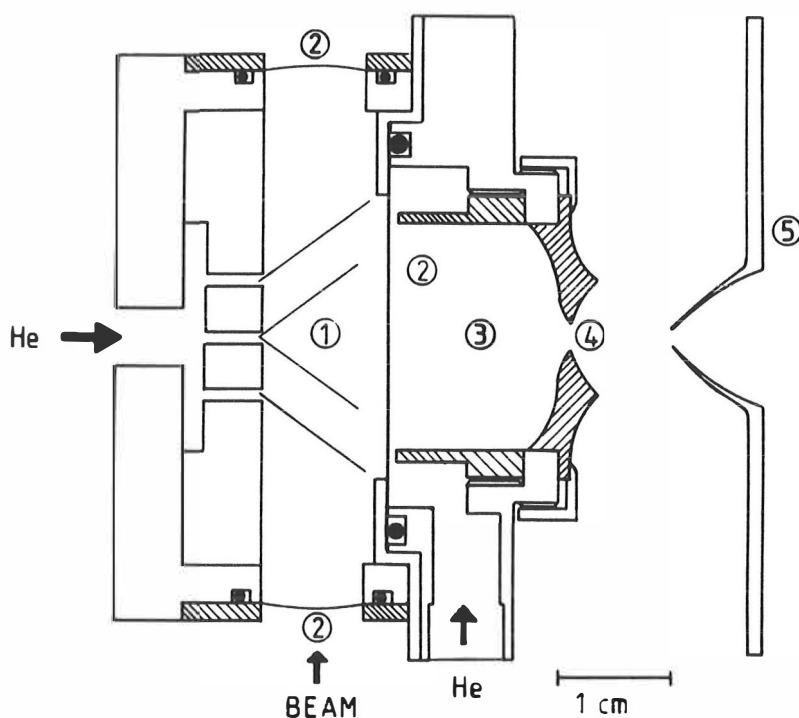
Figure 3.3   Schematic figure of the target chamber. (1) U-targets, (2) Windows (3) Stopping volume, (4) Exit hole, (5) Skimmer electrode.

3.2.2 Mass separation

The accelerated ion beam was focused by a pair of Einzel lens triplets to provide a parallel beam in the entrance of the mass separator. The mass separator was of the Scandinavian type with a 55° dipole magnet. The mass resolving power of about $M/\Delta M = 430$ was obtained with a typical setting in the ion guide as illustrated in Fig. 3.4. The first pair of horizontal and vertical slits was situated in the exit of the dipole magnet and the second one was situated about half a meter upstream from the focal plane of the dipole magnet, which was also the implantation point of the ion beam. The vacuum inside the separator was about 10^{-7} mbar and was achieved with three diffusion pumps having the pumping capacity of about 1300 l/s. In the end of the beam line the vacuum was kept on by applying a cold surface cooled down to the temperature of liquid nitrogen. In connection with the conversion electron measurements an additional ion optical element, namely the electrostatic X-Y-deflector, was added to the near end of the beam line to guarantee an optimal beam transfer into the conversion electron spectrometer. A movable, 1/4 inch wide tape was situated in the focal plane of the IGISOL-separator. The maximum speed of the tape was about 600 mm/s and the operational design of the tape drive included both the internal and external pulsing of the drive. The walls of the narrow vacuum chamber surrounding the implantation point have plastic windows. Transmission of the photons in a KX-ray region is about 90 % and the thickness of the windows is capable to preserve a 10^{-6} mbar vacuum inside the chamber. A movable Faraday cup was situated just before the implantation point. This was used to measure the current $^{129}Xe^+$ ions in the calibration procedure.
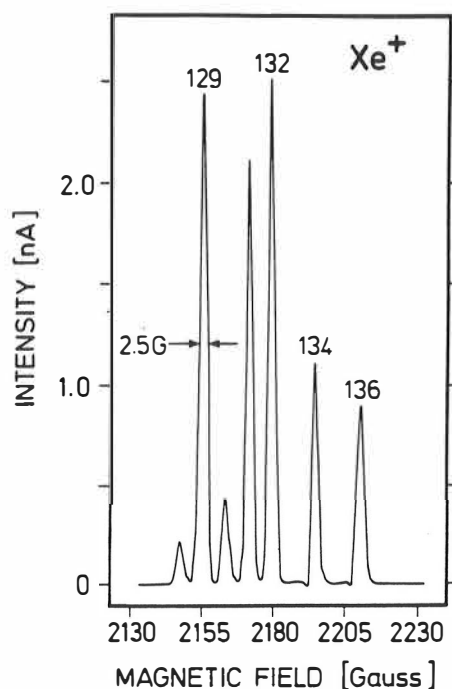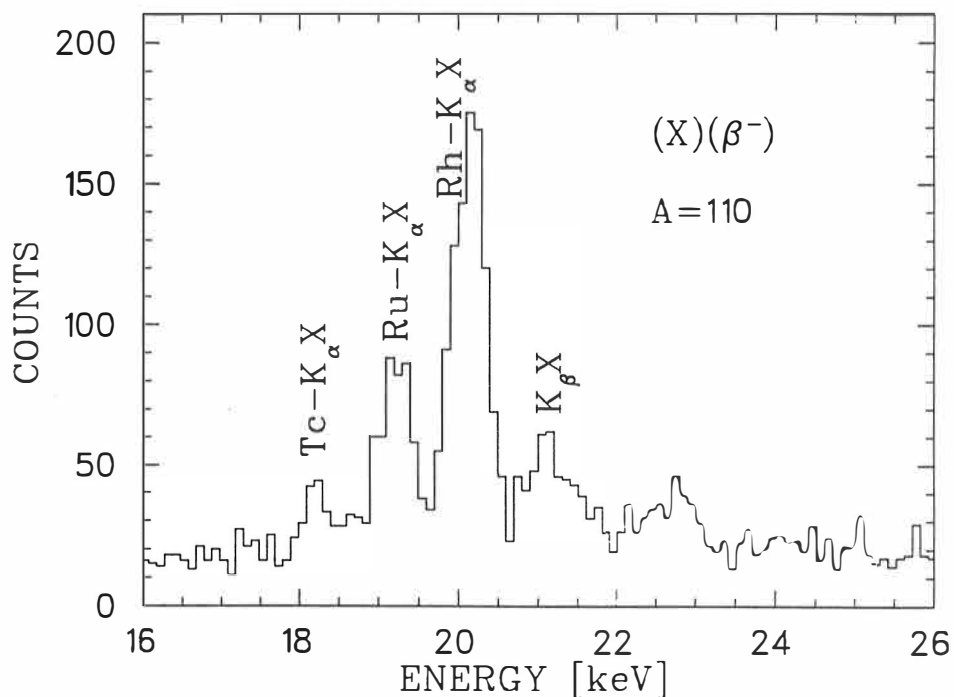

Figure 3.4

A mass spectrum of tracer gas of ^{nat}Xe. The distance between neighbouring masses is about 14 mm and the mass resolving power is about 430 measured at A=129.

3.2.3 Element identification

Due to the chemical non-selectivity of IGISOL, a whole mass chain of the isotopes is typically observed in the focal plane of the separator. The intensities of the different isotopes vary depending on the production yields and half-lives, but typically at least three different isotopes belonging to the same mass chain are observed. Fortunately, the internal conversion process, which is the source of a characteristic X-ray emission is favored in the region of interest, as was pointed out by W. Reisdorf *et al.* [Rei71]. For the unique identification of the isotopes, the characteristic X-ray emission has been used in combination with the mass separation. Use of the K X-rays as a source of identification is sometimes complicated because of the overlap of $K_\alpha X$ lines with $K_\beta X$ lines from $Z=Z-2$ elements. Fortunately, this is not a problem when very neutron-rich nuclei are studied due to the negligible production of lower Z isotopes. Figure 3.5 presents an example of the low energy region of photon spectrum at A=110. Three different isotopes were observed in focal plane of the IGISOL-separator.

Figure 3.5   Photon spectrum showing the K_α X-rays observed at A=110.

3.3 Spectroscopy methods

The analysis of beta feeding pattern is based on the intensity difference of the incoming and outgoing transitions. This requires a detailed knowledge of the decay scheme. The decay schemes of the studied nuclei are determined by using various experimental setups.

3.3.1 Basic setup for the beta-, gamma-, and X-ray spectroscopy

The aim of this setup is in the first case to identify new isotopes and the most intense γ-transitions belonging to the decay of a certain isotope by means of a coincidence with the characteristic X-rays. In the case of a pulsed experiment, a beta half-life connected to certain γ-transitions can also be extracted. In a few experiments, also the time spectra between different detectors were collected to measure the lifetimes of the excited states and to deduce the partial gamma half-lives. This setup allows also the determination of the conversion coefficients based on the fluorescence yield in a few favorable cases. In all experiments, the beta-detector has been a thin plastic scintillator detector with the thickness of either 0.75 or 0.9 mm. In the first experiments an X-ray detector used was a planar Ge-detector with an active volume of 1.4 cm^3. Later it was replaced by a planar low energy Ge-detector having an active area of 1000 mm^2 and thickness of 10 mm. Both of them possess good timing properties. Photons with higher energies were detected with a high-purity (HP) Ge-detector with the nominal efficiency from 20 to 50 percents. TDC-parameter records all events as a function of a time inside the measurement cycle. In addition to the energy signals and the TDC-spectrum, the time spectrum between X-ray and beta detector was recorded in most of the experiments. The time-spectra was analyzed by using a centroid shift method or a slope-method if possible. Although the time spectra between gamma and beta alone cannot provide the accuracy needed for the lifetime spectroscopy, it can be used for the identification of the lifetimes in the range of a nanosecond or more. An example of the typical detector geometry is presented in Fig. 3.6.a.

3.3.2 Conversion electron measurements

Due to the number of low-energy transitions characteristic for the level scheme of deformed odd-odd nucleus, a conversion electron emission plays an important role among the possible de-excitation modes of excited states. This also implies the importance of the determination of conversion coefficients. Conversion electron measurements applied the novel electron spectrometer, ELLI, which is specially designed for the IGISOL-separator [Par91]. It combines the high transmission of the two-coil magnetic transporter to the good energy resolution of a LN-cooled Si(Li)-detector. The original version of the ELLI-spectrometer was supplied with a Si(Li)-detector with 4 mm thickness and an active area of 200 mm^2. This detector was later replaced by a 4 mm thick detector with an area of 300 mm^2. Both of them

were used in the experiments of this thesis. The spectrometer is designed so that the ion beam of the IGISOL-separator can be implanted into the movable tape, which is situated in the central axis of the spectrometer inside one of the two coils. The emitted electrons are transported to the Si(Li)-detector, which in turn is situated inside another coil. The distance of the source and the detector reduces effectively the gamma-background due to the small solid angle. A second detector can be placed behind the implantation point providing a reasonable solid angle for another detector. Due to the magnetic field of ELLI-spectrometer a special type of Ge-detector with a nominal intensity of 20 % have been applied in simultaneous gamma and electron measurements. For beta and conversion electron measurements, the gamma detector was replaced with a Si(Au) surface barrier-detector with an active area of 450 mm^2 and thickness of 500 μm. In some experiments, a time spectrum between the conversion electron detector and another detector was collected.
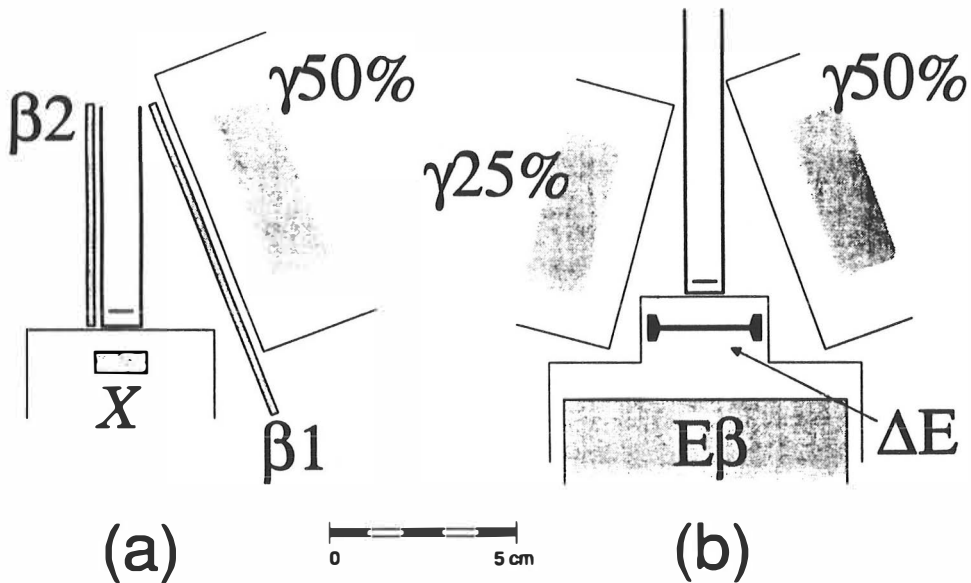
Figure 3.6 The detector geometry used for the conventional beta-, gamma- and X-ray spectroscopy (a) and for the decay energy measurements (b).

3.3.3 Data evaluation

In all experiments, the combination of a slow and a fast coincidence was used. The slow coincidence branch was used to trigger data acquisition due to its superior energy resolution as compared to the fast coincidence. This allows a precise tuning of the low level threshold for
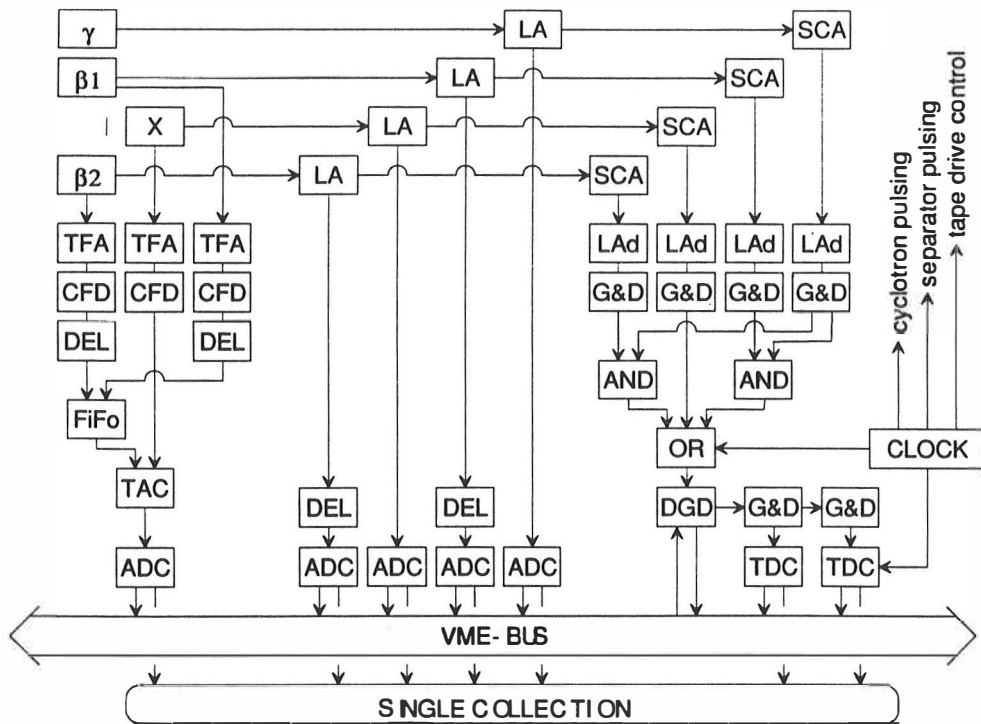
the trigger logic. A time window of an overlap coincidence was typically of the order of 2 microseconds. Besides the slow-coincidence, the fast coincidence was used to measure the time spectra between different detectors. In the off-line analysis, the time spectrum provides possibility to limit the coincidence window below 100 ns. However, this is not needed due to the slow counting rate of IGISOL-experiment.

Due to the different half-lives of the different isotopes in certain mass chain, a pulsing of the experiment plays an important role. The intensity of the wanted isotope as compared to others in the same isotopic chain can be enhanced by a proper choice of the pulsing of the experiment. In the simplest version, only the movable tape in the implantation point of the IGISOL-separator was pulsed to remove long-lived activities from the vicinity of the detectors. The IGISOL-separator itself can also be pulsed by using the electrostatic plates placed before a dipole magnet of the IGISOL-separator. This allows the pulsed experiment, where the collection of the activity in the implantation point is followed by the period, when ion beam of IGISOL is deflected off and the decay of the activity is registered. The beam on and beam off periods are repeated during the experiment. The ion beam of the cyclotron was pulsed simultaneously with the IGISOL-separator to reduce the background related to the proton beam.

In addition to the conventional half-life measurements, the pulsing of the experiments allows the estimation of the half-life by comparing the intensities of the beta-gated transitions in the in-growth and decay periods. Details are presented in the Appendix A1. Additionally, pulsing of the experiment plays an important role in the estimation of the ground state branching, as explained in Appendix A2.

In all experiments, data was collected in the event mode to magnetic tapes. The number of the parameters was limited to seven with a maximum resolution of 4096 channels. The energy parameters alone reserved two to four parameters leaving 3 to 5 parameters for the timing purposes. Besides the primary collection to the tape, the data flow was controlled by the on-line monitoring, which also included a few predefined gated spectra. Histograms of the on-line monitoring were stored frequently to a hard disk, where they were available for further analysis either during the experiment or afterwards. Additionally, all energy parameters were collected in a single mode and stored to the hard disk by using a separate data acquisition system. The events stored to the magnetic tapes included all energy signals and the time of the occurrence of the event. This parameter was used to remove those periods of the experiments, where something undesired had happened. It also provides an easy method for the gain shift correction if needed. Whenever the pulsing of the experiment was applied, also the time of the event inside the measurement cycle was recorded and stored. A block diagram of the measurement electronics is presented in Fig. 3.7.

γ → LA → SCA

β1 → LA → SCA

X → LA → SCA

β2 → LA → SCA

TFA TFA TFA
CFD CFD CFD
DEL DEL

FiFo
TAC
ADC

DEL DEL
ADC ADC ADC ADC

LAd LAd LAd LAd
G&D G&D G&D G&D
AND AND
OR ← CLOCK
DGD → G&D → G&D
TDC TDC

→ cyclotron pulsing
→ separator pulsing
→ tape drive control

VME- BUS

SINGLE COLLECTION

Figure 3.7   A block diagram of the measurement electronics used in the typical β-, X-, γ-, and TDC-measurement. Figure also shows the clock used for controlling the experiment. Following abbreviations are used: LA = linear amplifier, SCA = single channel analyzer, TFA = timing filter amplifier, CFD = constant fraction discriminator, LAd = level adapter, G&D = gate and delay generator, FiF0 = fan in - fan out, DEL = delay, ADC = analog-to-digital converter, TDC = time-to-digital converter.

3.4   Decay energy measurements

The decay energy measurements were done with a setup consisting of two high-purity (HP) Ge-detectors and a ΔE-E-telescope for beta-particles. The detector geometry is presented in Fig. 3.6.b. In the study of $^{108\text{-}114}$Ru-isotopes, HP Ge-detectors with a nominal efficiency of 20 % and 25 % were applied to gate signal from the ΔE-E-telescope. In the Mo and Zr experiments, the 20 % Ge-detector was replaced with a 50 % HP Ge-detector to maximize detection efficiency. At the same time with the decay energy data, gamma-gamma-coincidence events were also collected. This setup provides also a possibility to energy selective beta-gating. This method reduces efficiently the intensity of the transitions belonging to decay of the lighter nuclei in the same mass chain. This technique has been applied for instance in the study of the collective structure of ^{110,112}Tc-isotopes [Äys90]. In the case of the decay energy

measurements, the tape drive alone was cycled to remove the long-lived daughter activities. The cyclotron beam as well as the IGISOL-separator were operated in the continuous mode to maximize the yield of the nuclei studied.

The ΔE-E-telescope for beta particles consists of a Si(Au)-surface barrier detector and a BC-400 plastic scintillator cube. The ΔE-detector rejects gamma-radiation and defines the aperture of the telescope. The estimated geometrical efficiency of the telescope was about 6 %. The ΔE-detector used was 500 μm thick and had an active area of 300 mm^2. The calculated energy loss of beta particles in the ΔE-detector is about 190 keV along the trace perpendicular to the surface of the detector. The E-detector has a cylindrical shape with the height of 60 mm and diameter of 75 mm. Due to the size of the detector, the maximum energy of beta-particles, which can be stopped at the detector, is about 10 MeV. This is clearly more than the endpoint energies measured in this thesis. The energy loss of beta-particles in the ΔE-detector and the window material were calculated according to the equations of Ref. [Trz89]. The calculated total energy loss was almost constant, of the order of 210 keV, in all material between an implantation point and the E-detector. The energy loss in the ΔE-detector was about 190 keV in the energy range from 600 keV to 6 MeV. The scintillator cube was capsulated inside of an Al-cylinder having open ends. The plastic detector was coupled to a photo cathode of a RCA-photo multiplier by using an optical grease and the other end of Al-cylinder was covered with an Al-foil having thickness of 3 mg/cm^2. The photo multiplier was shielded with μ-metal from the magnetic field. An energy dependent signal of photo multiplier was taken from the dynode. The anode signal was used for timing purposes. The timing signals of the ΔE and E detectors were used in off-line analysis to reduce the overlap coincidence window between ΔE and E-detector to 40 ns.

The ΔE-E-telescope was calibrated with the activities produced at the IGISOL-separator. This provides equal conditions as compared to the measurements of the unknown beta-spectra. The calibration activities used were ^{125}In, ^{125}Sn, ^{99}Y, ^{99}Zr, and ^{99}Nb. In addition, the standard beta sources of ^{106}Rh and ^{90}Y were used when tuning the detectors. Altogether 7 calibration points were collected in the energy range from 2 MeV to 7 MeV. A list of calibration activities is presented in Table 3.1.

The analysis of beta-spectra was carried out by using the shape fitting method described in Ref. [Dav76]. In the fitting procedure the standard shape of the beta spectrum was taken from the one-component beta-spectra of which endpoint energy was known with good accuracy. In the fitting procedure the program varied two free parameters, which alter the height and either stretch or compress the standard shape along the abscissa until the χ^2 minimum is reached. After determining the standard shape, the fits were performed on the single component beta-spectra of the other calibration activities. The linear least square fit was then used as an energy calibration for the specified stretch factors. Due to the element and energy dependence of the

shape of the beta spectrum, the calibration activities were chosen from the vicinity of the studied isotopes. Additionally, energy dependence was taken into account by applying different standard shapes in different energy ranges.

Table 3.1 The calibration activities of the decay energy measurement. All energies are given in keV.

	Q_β	$E\gamma$	E^*	E_β	Ref.
^{99}Y	7568(14)	930,1014	1589	5979(14)	[Gro92]
		724	724	6844(14)	
^{99}Zr	4559(13)	56,546	1015	3544(13)	[Gro92]
^{99}Nb	3640(13)	98,137	236	3405(13)	[Wap85]
^{125}In	5480(80)	745,1335	1363	4118(80)	[Ale78]
		188	215	5445(80)	
^{125}Sn	2350(8)	332	332	2018(8)	[Wap77]
^{106}Rh	3540(9)	622,1134	1134	2406(9)	[Wap85]
^{90}Y	2282(3)	-	0	2282(3)	[Wap85]

4 Experimental results

Experimental details of the decay studies of Ru and Mo isotopes are presented in Papers I and III-V. They included a conventional β-, γ- and X-ray spectroscopy setup, decay energy measurements and conversion electron spectroscopy. The obtained information, decay energies, half-lives and decay schemes, were used for determination of the experimental beta-strength according to equation

$$B_{\Sigma}(GT) = C\left\{\left(\frac{g_A}{g_V}\right)^2 \sum_{i=0}^{Q} f\left(Z, Q_\beta - E_i\right) t_{1/2}(i)\right\}^{-1},$$

(4.1)

where (g_A/g_V) is the ratio of the axial vector and the vector coupling constants. This was taken as 1.263 according to Ref. [Tow85]. The value of the constant C of 6160 s was used. The phase space factor $f(Z,Q-E)$ is tabulated in [Gov71]. Due to the very steep dependence of $f(Z,Q-E)$ function from the beta energy available, an accurate decay energy is crucial for the precise estimation of the experimental Gamow-Teller strength.

The individual partial half-lives of the beta decay were deduced from the equation

$$t_{1/2} = \frac{T_{1/2}(\beta^-)}{I_\beta},$$

(4.2)

where I_β is a beta feeding of the excited state in question. Beta feedings of excited states, in turn, are deduced from the intensity difference of the incoming and outgoing total transition intensities.

The average energy of the 1^+ states, $E_{ave}(1^+)$, serves as a simple measure of the position of the beta strength distribution if the weight of the averaging is taken from the individual beta transition strengths. A corresponding equation for the beta strength weighted average of the excitation energy $E_{ave}(\beta)$ can be written as

$$E_{ave}(\beta) = \frac{\sum_i S_i(\beta) E_i}{\sum_i S_i(\beta)}.$$

(4.3)

The value of $E_{ave}(\beta)$ is dominated by the energies of 1^+ states due to the order of magnitude higher beta strength associated to allowed transitions as compared to hindered transitions. As a result, an experimental $E_{ave}(\beta)$ is used when compared to theoretical calculations.

38

4.1 Previous results

4.1.1 Shell model Cd-nuclei and γ-soft Pd-nuclei

Since neutron-rich Pd isotopes provide a less deformed reference for the studies of this thesis, the experimental data concerning them are also briefly summarized in this chapter. The study of beta decay properties was initiated at the IGISOL-facility by measuring the decay properties of even-A $^{114-118}$Pd isotopes [Kop89]. These studies were continued on ^{118,120}Pd [Jan93]. In addition, [Fog90] reports on the decay study of $^{113-116}$Pd. The decay energies of ^{114,116}Pd are based on the latter reference. The decay scheme of ^{112}Pd is based on that presented in [DeF89]. The partial decay schemes of n-rich Cd-isotopes are already presented in Fig. 1.1. They demonstrated one strong beta transition with very low logft-values. The decays of Pd-isotopes reveal the role of the configuration mixing and residual interactions. Instead of the one strong $0^+\rightarrow1^+$ beta transitions, the decay of Pd-isotopes includes few $0^+\rightarrow1^+$ beta transitions having slightly higher logft-values as compared to Cd-isotopes.
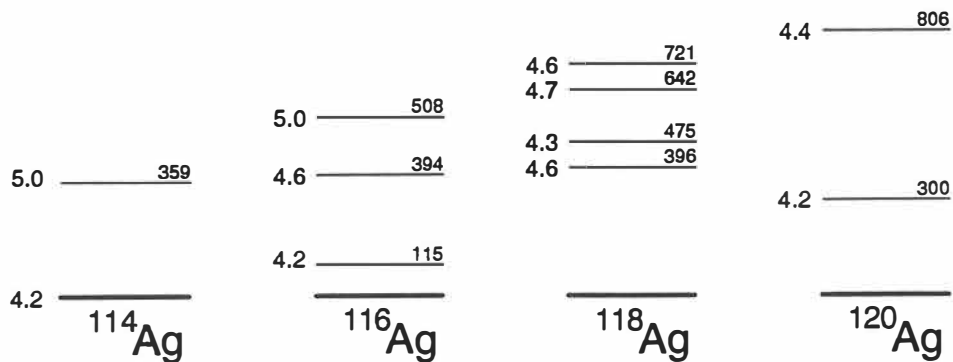
Figure 4.1   The final states of allowed beta decay of $^{112-120}$Pd-isotopes based on the experimental data in Refs. [DeF89,Kop89, Fog90,Jan93].

The collective properties of even-even nuclei are well characterized by their level schemes. The excited levels in the neutron-rich Pd-isotopes were studied at the IGISOL-facility via the beta decay of Rh-isotopes [Äys88]. According to Ref. [Äys88] neutron-rich Pd isotopes possess large softness against deformation, but the question of the degree of the deformation remains unanswered.

4.1.2 Triaxial Ru-isotopes

The level schemes of the neutron-rich Ru isotopes have been studied by using the various experimental methods. The beta decay studies of ^{106,108}Tc isotopes are reported in Ref. [Süm80]. These studies applied the thermal neutron induced fission of ^{239}Pu and a chemical separation technique SISAK [Ska80]. In [Süm80], the experimental data was compared to the various theoretical calculations. A similar study of the collective structure of ^{110,112}Ru was carried out at the IGISOL-facility [Äys90]. In addition, Ref. [Sta84] reports on the $(\gamma)(\gamma)$ directional measurement leading to the assignment of the spins and parities of the most of the excited states in ^{106,108}Ru. In Ref. [Dur89] a Ge-array was applied in the study of the prompt γ-radiation from the primary products of the spontaneous fission of ^{252}Cf. In this article the rotational ground state bands were established up to spin 10^+ for even-A $^{104-112}$Ru isotopes. Recently, a similar study has been done by using the EUROGAM Ge-array resulting in the observation of the rotational ground state band in ^{114}Ru [Phi94]. All these studies imply the large β deformation for the neutron-rich Ru-isotopes. Additionally, increasing neutron number seems to be connected to developing γ-softness. All in all, the γ-softness of the Ru-isotopes is suggested rather than a rigid rotor.

4.1.3 Well deformed Mo-isotopes

Shapes of the Mo-isotopes have been a subject of various articles. In Ref. [Hot91] the spontaneous fission source of ^{248}Cm was situated inside the array of the Compton-suppressed Ge-detectors and the rotational bands of the $^{102-108}$Mo were identified. In general, the deformation of the even-A Mo-isotopes was observed to increase with the increasing neutron number so that the maximum is reached at the neutron number N=64. The obtained rotational bands were observed to exhibit the characteristics of a good rotor up to the highest observed spins. The shapes of the ^{102,104}Mo isotopes were studied in [Lia91] via the beta decay of ^{102,104}Nb isotopes. They also measured the lifetime of the first $2^+ \rightarrow 0^+$ transition leading to the quadrupole deformations β of 0.28(1) and 0.31(2) for ^{102}Mo and ^{104}Mo, respectively.

4.2 Decay studies of even-A $^{108-114}$Ru and $^{106-110}$Mo isotopes

The decay studies of even-A Ru-isotopes are reported in Papers I and III. Prior to this work, the experimental information of ^{110}Ru included two gamma-rays [Fra78] and a half-life of beta-decay [DeG83]. A beta half-life of ^{112}Ru was reported incorrectly in [Fra78] and no information concerning the decay of ^{114}Ru was published. Studies of this thesis included the construction of the decay schemes of ^{110,112,114}Ru isotopes and the decay energy measurements of ^{108,110,112,114}Ru isotopes. The decay energies of Ru-isotopes are reported up to A=109 in Ref. [Gra89]. The most neutron-rich Ru-isotope, whose decay scheme has

been reported is ^{113}Ru [Pen92]. Partial decay schemes of the ^{108,110,112,114}Ru isotopes as obtained in this study and according to Ref. [Pie62] are presented in Fig. 4.2.
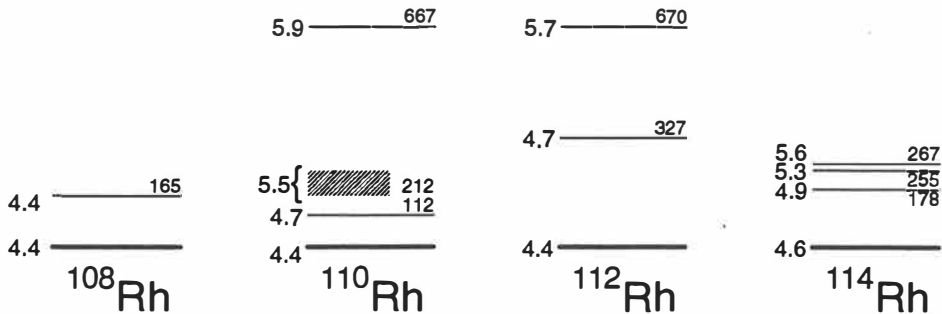
Figure 4.2   The final states of allowed beta decay of $^{108-114}$Ru isotopes.

Beta decay of lighter Mo-isotopes, ^{102,104}Mo are reported in Refs. [DeG79,DeF91, Gra87,Bla91], which are a source of the experimental data used in this work. Decays of ^{106,108}Mo were reported in Paper V and the decay of ^{110}Mo was shortly discussed in the same article. The decay scheme of ^{106}Mo is reported in [DeF88] and decay energy of ^{106}Mo is measured by [Gra89]. Prior to this thesis, the decay scheme of ^{108}Mo has not been published. The decay energy of ^{108}Mo was reported also by [Gro92], but no information was given concerning the decay scheme or γ-transitions used for the gating. Prior to this work, there was no experimental information about the ^{110}Mo-isotopes.
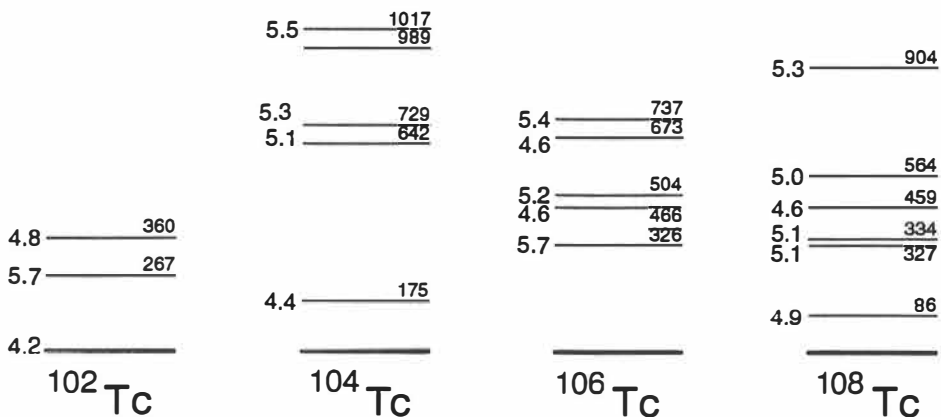
Figure 4.3   The final states of allowed beta decay of $^{104-108}$Mo isotopes.

4.3 Decay energies and half-lives

Since the first experiments using the fission reaction, the IGISOL-facility has produced a vast amount of new half-life data in the Zr-to-Pd-region. Typically the half-lives are based on the decay curves of the identified gamma-transitions in coincidence with beta-particles. Paper II reports the newest half-lives measured at the IGISOL-facility, which are presented in Table 4.1. In these studies, the enhanced X-ray emission was applied by measuring the decay curves of beta gated KX-lines. This provides both the unique element identification and the beta half-life. In Paper IV, all new half-lives are included in the comparison to various half-life predictions. Since 1991 experiments, a new experiment has been initiated at the improved IGISOL-facility at the new Accelerator Laboratory. Due to the higher intensity and higher energy of a proton beam, the production of ^{110}Mo was increased by order of magnitude. The analysis of the data was started when finishing this thesis. The preliminary results indicate that the half-life reported in Paper II was slightly too short, although correct within error bars. A new value of 300(40) ms is obtained and is also included in Table 4.1.

Table 4.1   New half-lives measured at the IGISOL-facility.

Nucleus	Half-life [ms]	Nucleus	Half-life [ms]
^{105}Zr	1000^{+1200}_{-400}	^{110}Mo	300(40)
^{107}Nb	330(50)	^{113}Tc	130(50)
^{109}Mo	530(60)	^{115}Ru	740(80)

In addition to the new half-lives, many new decay energies of Pd, Ru, and Mo isotopes have been measured at the IGISOL-facility. In the following Table 4.2, the decay energies of Ru and Mo-isotopes, two neutron separation energies and mass excesses are listed. The decay energies of Pd-isotopes are reported in Refs. [Kop89,Jan93] and details of the endpoint energy measurement of Ru and Mo-isotopes can be found in Papers I, III and V and references there in.

The main purpose of this work has been the study of beta decay properties. The experimental details are presented in Papers I, II, IV and V. The decay properties of Pd, Ru and Mo isotopes are summarized in Table 4.3 below. In addition to the obtained decay energies and half-lives Table 4.3 includes the total beta strengths and effective log ft values. Additionally, the experimental average energies of the excited states have been included in the last column of the table.

Table 4.2 The decay energies of the neutron-rich Pd, Ru and Mo-isotopes. Decay energy of ^{110}Mo is extrapolated based on the relation between the half-lives and the decay energies of even-A $^{102-108}$Mo-isotopes. All numbers are given in MeV.

|	Q_β	S_{2n}	Mass excess
^{114}Pd	1.451(25)	13.300(30)	-83.494(25)
^{116}Pd	2.62(10)	12.600(60)	-79950(50)
^{118}Pd	4.1(2)	11.73(23)	-75.540(220)
^{120}Pd	~ 5.5(1)	10.9(10)	-70.270(1000)
^{108}Ru	1.35(6)	14.13(12)	-83.660(120)
^{110}Ru	2.81(5)	12.63(26)	-80.140(230)
^{112}Ru	4.52(8)	11.62(56)	-75.620(510)
^{114}Ru	6.12(20)	11.42(74)	-70.890(540)
^{104}Mo	2.16(4)	12.920(60)	-80.330(60)
^{106}Mo	3.520(17)	12.630(90)	-76.257(22)
^{108}Mo	5.12(4)	10.69(15)	-70.820(160)
^{110}Mo	~ 6(1)	10.4(11)	-64.860(1080)

Table 4.3 Beta decay properties of neutron-rich Pd, Ru, Mo isotopes.

Nuclide	$T_{1/2}$ [s]	Q_β [MeV]	log ft	B(GT)	$E_{ave}(\beta)$
^{114}Pd	145(9)	1.451(25)	4.14(6)	0.28(4)	37
^{116}Pd	10.8(2)	2.62(10)	3.93(3)	0.45(4)	205
^{118}Pd	1.9(1)	4.1(2)	3.90(13)	$0.49^{+.18}_{-.13}$	538
^{120}Pd	0.5(1)	~ 5.5(1)	<3.97	>0.42	>504
^{108}Ru	273(3)	1.35(6)	4.17(9)	$0.26^{+.06}_{-.05}$	98
^{110}Ru	11.6(6)	2.81(5)	4.18(6)	$0.26^{+.04}_{-.03}$	54
^{112}Ru	1.75(7)	4.52(8)	4.23(5)	0.23(3)	135
^{114}Ru	0.57(5)	6.12(20)	4.35	0.17	95
^{102}Mo	687(12)	1.010(23)	4.09(5)	0.31(4)	77
^{104}Mo	60(2)	2.16(4)	$4.13^{+.05}_{-.06}$	0.29(4)	382
^{106}Mo	8.73(10)	3.520(17)	4.18(2)	0.258(13)	525
^{108}Mo	1.09(2)	5.12(4)	4.14(3)	0.28(2)	396
^{110}Mo	0.30(4)	~ 6(1)			

5 Discussion

5.1 Half-lives

A new half-life data measured at the IGISOL-facility is compared to various half-life predictions in Fig. 5.1. The models were already presented in Chapter 2. The vertical axis presents the ratio of the calculated and experimental half-lives. A horizontal axis corresponds to the mass number A and the data points are grouped according to element number. Predictions of the models are commented below.
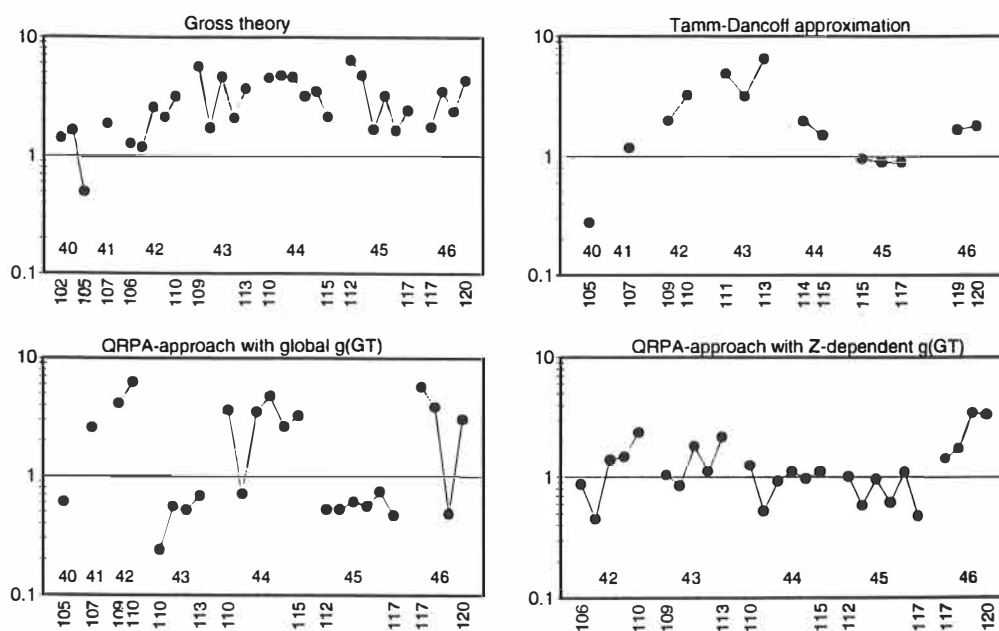
Figure 5.1 Comparison of the experimental and theoretical half-lives. Figure presents the ratio of theoretical and experimental half-lives for neutron-rich isotopes of elements from Zr to Pd.

Gross theory. The oldest predictions based on the Gross theory of beta decay tends to overestimate the half-lives in this region. The predicted half-lives are about three times too long as compared to the experimental ones. Deviation is largest for the Ru and Rh isotopes and smallest for the Zr-isotopes, which correspond to the well known proton subshell closure $Z=40$. Similar results were also obtained among the very light fission products in the vicinity of the proton p-shell closure at $Z=28$ [Ber90] and also in the heavy fission products at rare

earth region with $A>150$ [Gre88]. In [Ber90] half-lives of the neutron-rich Co ($Z=27$) and Cu ($Z=29$) were overestimated, but the calculated half-lives of the Ni-isotopes ($Z=28$) agreed with the experimental ones. Comparison in the Fig. 5.1.a and the results of [Ber90] imply that this model is better suited for the nuclei near the closed shells, but it tends to overestimate the half-lives between the closed shells. This in turn might be a result of excluding the collective effects and detailed nuclear structure, which are important outside of the closed shells.

TDA model of H.V. Klapdor et al. Although this model was proposed to take into account the collective effects better than the previous one, results imply just the opposite. Comparison in Fig. 5.1.b indicates poor agreement in the midshell and all in all the deviation from the experimental half-lives is relatively large. [Ber90] reports the overestimation of the half-lives before the closed shell and underestimation above the closed shell. Among the heavy fission products, this model mainly underestimates the half-lives [Gre88]. Summarizing, this model seems to result in random variation without clear connection to, for instance, the shell structure or collective properties of the nuclei.

QRPA-model of P. Möller et al. presents better agreement but the fluctuation is rather high. The ratio in Fig. 5.1.c indicates serious odd-even staggering (of the order of one magnitude) as related to the element number. However, for each element the ratio presented in Fig. 5.1.c is almost constant.

QRPA-model of A. Staudt et al. Comparison of the QRPA-model of A. Staudt *et al.* and the previous one illustrates the effect of the Z-dependent coupling constant of GT-residual interaction. Odd-even staggering of the previous model disappears totally. However, one may argue that the good agreement between prediction and experimental results has been achieved with an artificial parametrization of the model.

The theoretical models above, except the TDA-model, have to rely on the mass predictions in the regions where the decay energies are not known. According to power law [Tak73], the relation between the beta decay energy and the fermi function is as strong as $f=(Q-E)^5$. This rule implies that the modest change in the decay energy might result in large variation of the half-life predicted. This is demonstrated in Fig. 5.2, which shows the ratio of the calculated and measured half-lives of ^{110,112,114}Ru-isotopes with three different atomic mass predictions. With a proper choice of the mass prediction, a relatively good agreement between theory and experiment is achieved. When the same model is applied by using the decay energies of this work, even better agreement is achieved. This implies the importance of the decay energy measurements far from the valley of stability.
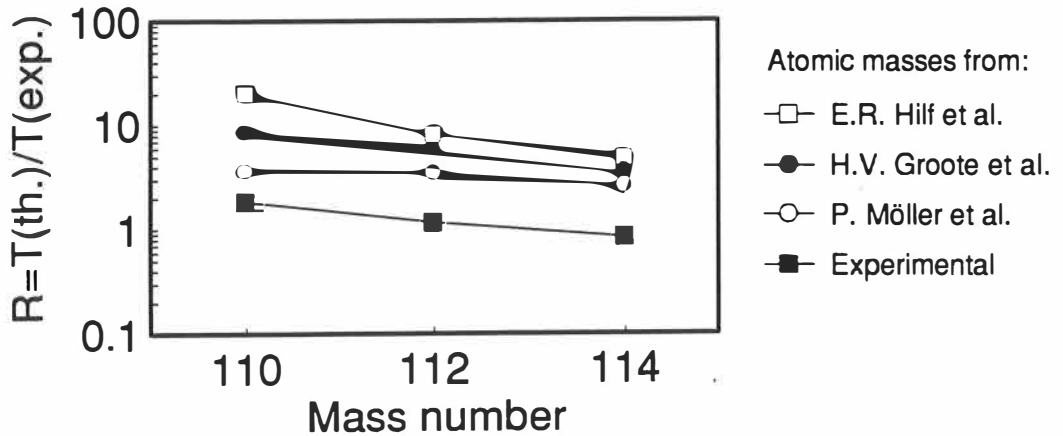
Figure 5.2 Relation of the half-life predictions and decay energies. Figure shows the half-life predictions of ^{110,112,114}Ru with three different choice for the mass predictions and same predictions when experimental decay energies of this thesis are applied.


5.2 Binding energies

5.2.1 Decay energies

The decay energies listed in Table 4.2 agree nicely with the predicted decay energies as illustrated in Fig. 5.3. However, in all cases (Z=46,44,42) the experimental results are relatively low as compared to predictions near the stable isotopes. When going further from the stability line, the experimental decay energies of each isotopic group possess steeper rise as compared to the predicted decay energies. The ETFSI-approach of J.M. Pearson *et al.* [Abu92] seems to follow best the steep rise observed. As a result, this model can be recommended for the extrapolations in the region of this study. The DM-based macroscopic-microscopic model of P. Möller *et al.* [Möl93] reproduces the decay energies of lighter nuclei for each element but fails to predict the heavier ones. This is evident for the Mo-isotopes, where the prediction of this model changes drastically above neutron number N=66.

### 5.2.2 Mass excesses of various atomic mass predictions

The mass excesses of the Pd, Ru and Mo isotopes are compared to various atomic mass predictions in Figs. 5.4, 5.5 and 5.6, respectively. In all figures, the difference of the calculated and experimental mass excesses, $\Delta m_e = m_e^{calc.} - m_e^{exp.}$ are presented as a function of neutron number. If the Δm is positive (negative), then the predicted binding energy of nucleus is

smaller (larger) than experimentally obtained binding energy. Experimental data in Figs. 5.4-5.6 combine the results of this work and the mass excesses of lighter isotopes reported in Refs. [Gra89,Gro92]. The mass excess of the daughter nucleus has been taken from the recent atomic mass table of G. Audi *et al.* [Aud93].
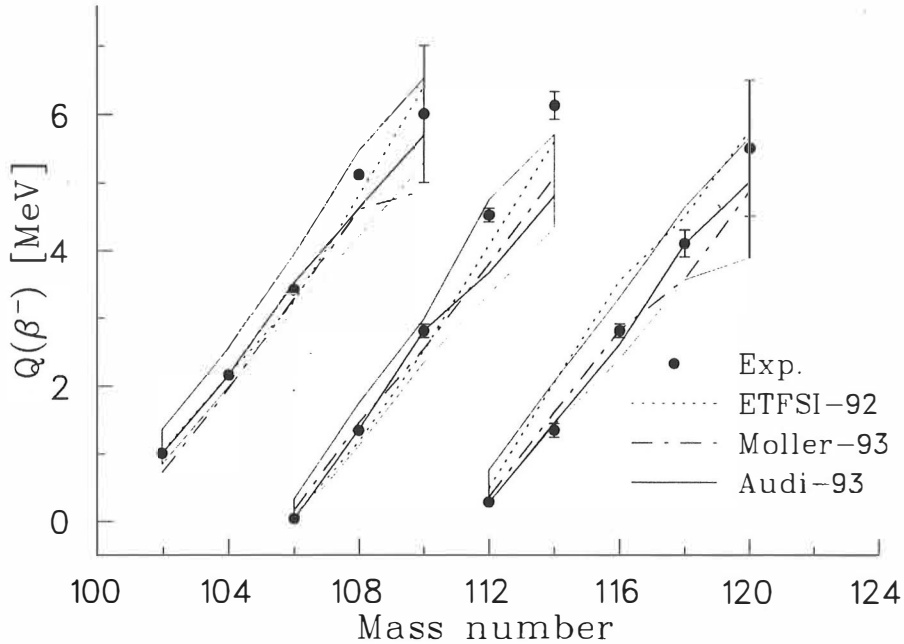

Figure 5.3 Comparison of the decay energies of certain predictions of the 1988 mass compilation for Pd, Ru and Mo-isotopes. Shaded regions present the range of the decay energy predictions in the 1988 atomic mass compilation [Hau88].

On the average, atomic mass predictions do not reveal any serious deviations except a model of Satpathy and Nayak for the heavier Ru-isotopes, as illustrated in Fig. 5.5. The overall agreement is more or less what can be expected due to fact that the studied nuclei are still close to the nuclei, which are used for parametrization of the models. A large number of parameters and short distance of the extrapolation should result in good agreement. On the other hand, this condition might lead to serious divergence when predictions are extended further away from known nuclei. The observed deviations are larger than the obtained ones for Sn, In, and Sb isotopes in the vicinity of doubly magic ^{132}Sn nucleus [Stö90]. This indicates that the predictions are more reliable near the closed shells. Due to the fact that shell corrections are negligible near the closed shells it is evident that the macroscopic part of the binding energy is understood well in the models and the deficiencies far from the closed shells come mainly from the shell correction or pairing terms. This is also supported by the decay studies in the rare-earth region, where larger deviations are also observed [Gra86,Gra90].
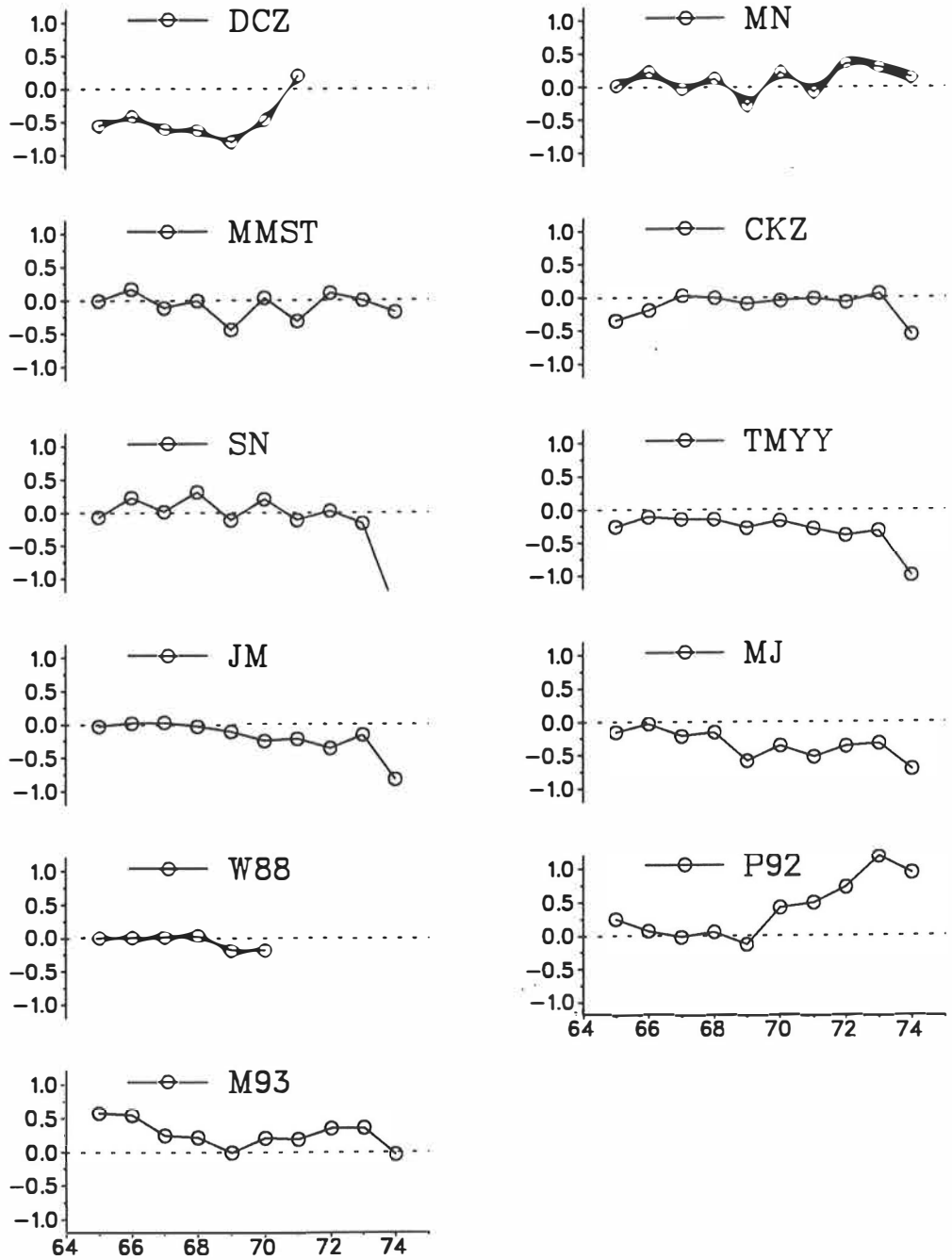
Figure 5.4 The experimental and predicted mass excesses of Pd isotopes. Difference of the calculated and experimentally obtained mass excesses are presented as a function of the neutron number.
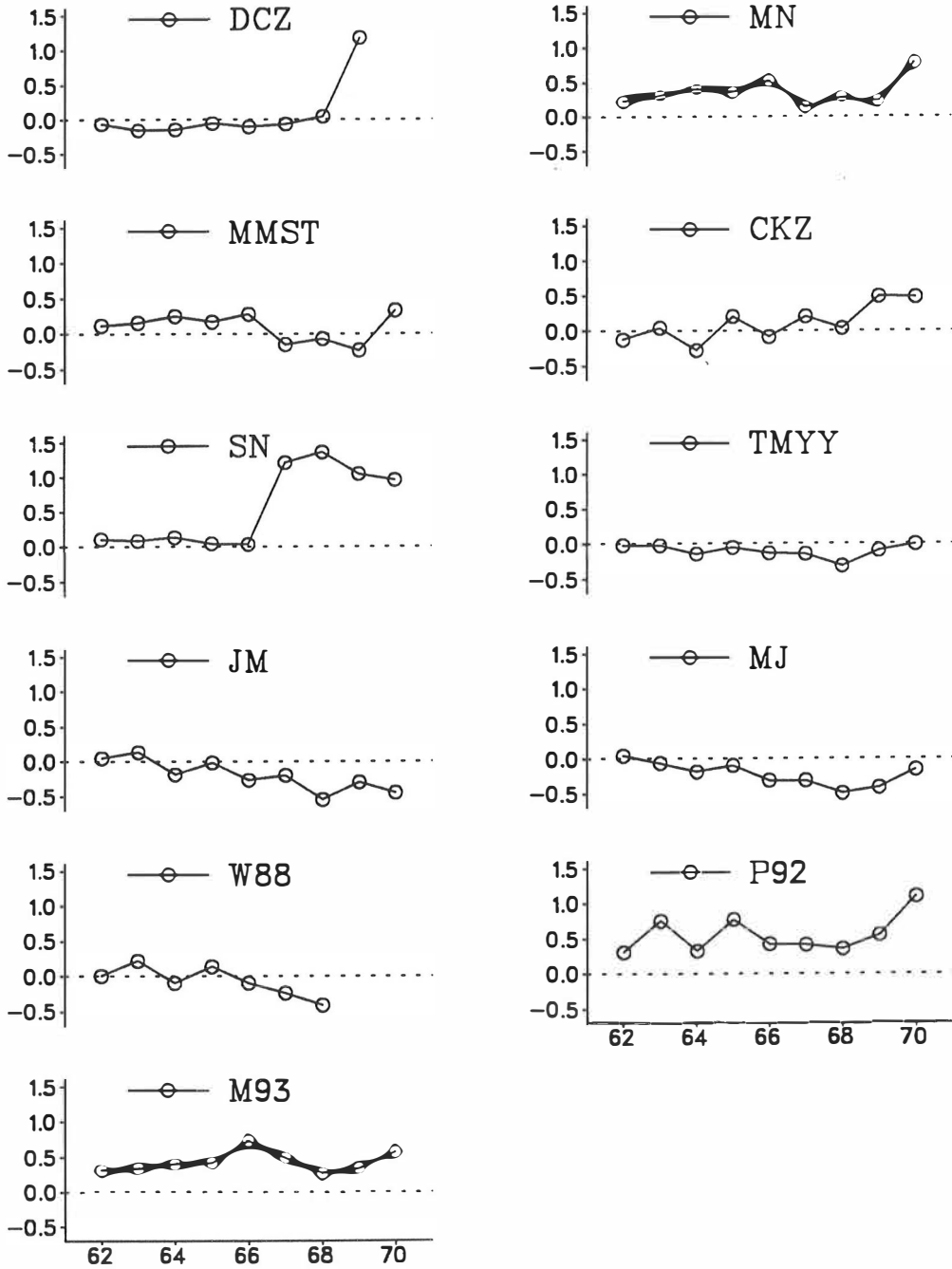
Figure 5.5 The experimental and predicted mass excesses of Ru isotopes. Difference of the calculated and experimentally obtained mass excesses are presented as a function of the neutron number.
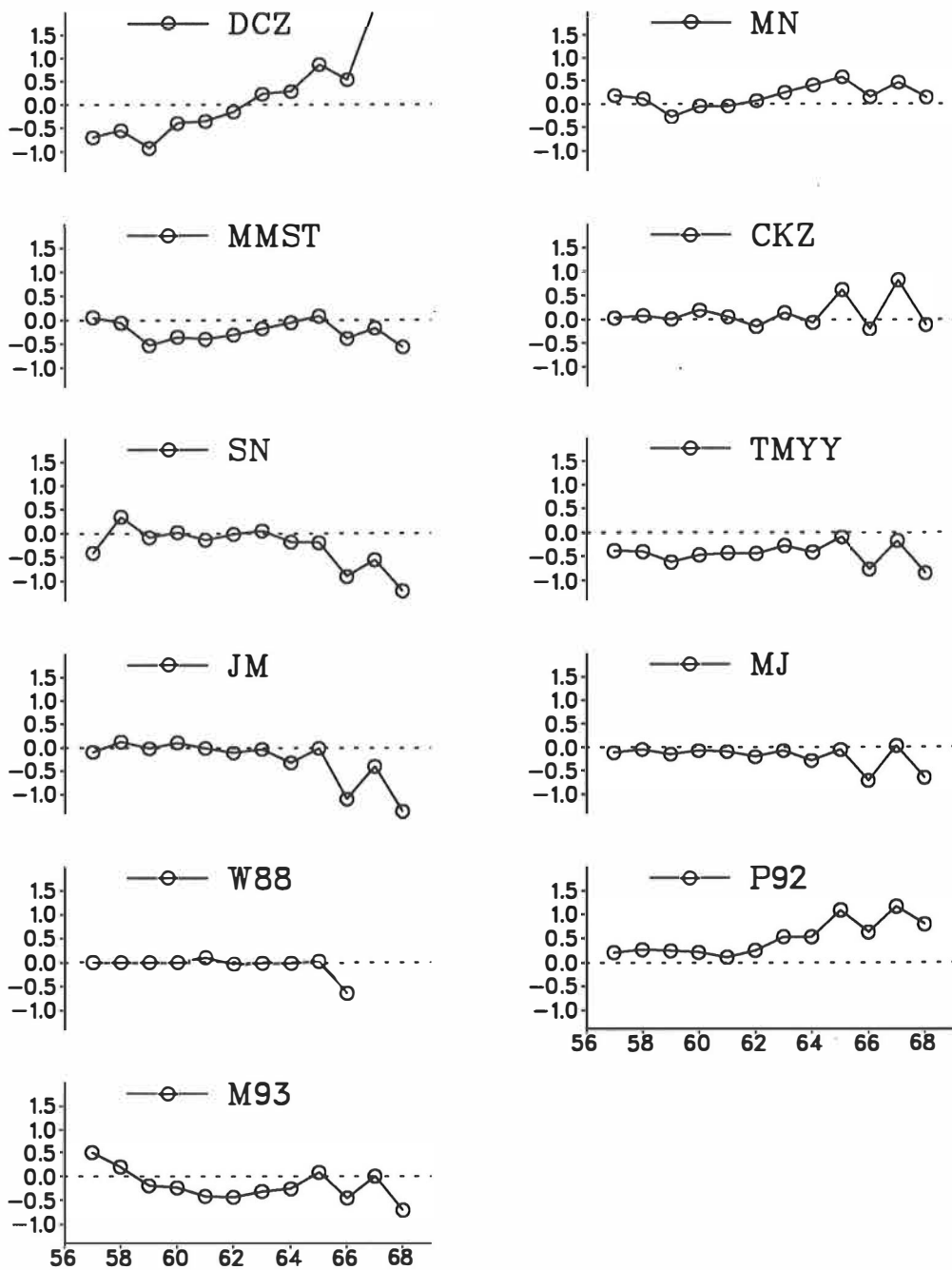
Figure 5.6 The experimental and predicted mass excesses of Mo isotopes. Difference of the calculated and experimentally obtained mass excesses are presented as a function of the neutron number.

50

5.2.3 Two neutron separation energies

Two neutron separation energy is smoothly varying with the neutron number except in the vicinity of the closed shells. Discontinuities in the S(2n) systematics are reliable indicators of the sudden changes in the binding of the nucleus. This, in turn, reveals the changes in nuclear structure. Figure 5.7 presents two neutron separation energies of the nuclei studied. The figure demonstrates the neutron subshell closure N=56, which is indicated by the sudden decrease of S(2n) values between neutron numbers N=56 and N=58. In Ref. [Gra89] it was explained as a mutual support of the subshell closures N=56 and Z=40. The figure shows also the increase of the S(2n) values at neutron number N=60. This increase is especially strong for Zr-isotopes [Pah84]. This indicates the onset of the deformation for isotopes with N≥60. Irregular behavior of the S(2n)-values with $37 \leq Z \leq 39$ is associated to complicated nuclear structure effects, which are obtained in various experiments [Bal92]. In Ref. [Gra89] the onset of deformation was related to all nuclei below Z≤45. The studies of this thesis indicate that the filling of N=66 neutron shell do not play any role for the Ru-isotopes. This is based on the continuos decrease of the S(2n)-values for heaviest Ru-isotopes as illustrated in Fig. 5.7. In the case of Mo-isotopes, the S(2n) systematics shows a kink upwards after N=66. This implies that the filling of the N=66 subshell closure is still important in the case of Mo-isotopes.
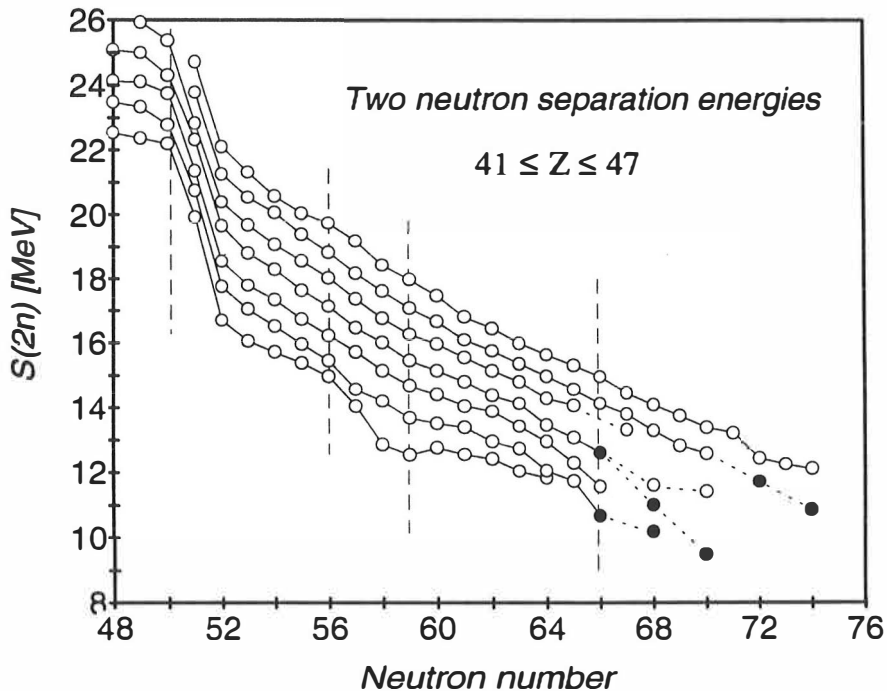
Figure 5.7   Two neutron separation energics from Nb (Z=41) to Cd (N=47) with Z=48-74.

5.3 Beta decay properties and deformation

In order to study the relation of the beta decay and deformation, the macroscopic microscopic model was applied. The calculated average energy of 1^+ final states inside the decay energy window and the experimental average energy of excited states are presented in Figs. 5.8-5.10. The calculations are divided into the oblate and prolate cases. For Pd-isotopes, also spherical calculations were performed due to the small deformations and deformation energies as presented in Table 2.4. Figures 5.11 and 5.12 present the calculated two-quasi particle 1^+ states and GT-strengths for the $^{110-114}$Ru and $^{104-108}$Mo isotopes, respectively. The figures on the left represent the oblate final states and on the right are the calculated prolate final states. The figures in the middle column contain the experimental beta-strength distributions. In addition, calculated distributions are supplied with sensitivity limits, which correspond to 0.5 % beta feeding. In the following, the results are commented isotopic-wise:

Palladium isotopes. Calculations for the Pd-isotopes are presented here for the reference for the Ru and Mo-isotopes. The experimental data of the Pd-isotopes are based on the Refs. [Kop89,Fog90,Jan94]. Due to the fact that the deformation energies and deformations are relatively small, also the spherical calculations are included. As far as average energy is concerned, the spherical calculation reproduces the observed systematics of $E_{ave}(\beta)$ especially in the case of $^{112-116}$Pd. Above ^{116}Pd, calculated $E_{ave}(1^+)$ shift upwards rapidly due to the strongly fed states in the top of the calculated decay energy window. In the case of ^{118}Pd, the calculated states are lying above the experimental decay energy. When this is taken into account, the high lying states do not contribute to the average energy $E_{ave}(1^+)$ and its value decreases to the level of 1.3 MeV. In the light of this comparison the large oblate deformations are excluded ($\beta < -0.15$). Most of the strength observed in small deformations is related to $g_{7/2}$ and $d_{5/2}$ shell model and $d_{5/2}$ and $g_{9/2}$ proton states. Especially, the coupling of 7/2[404] and 9/2[404] tends to drive the shape of the nucleus to spherical one. Same was observed for the Ru and Mo-isotopes.

Ru-isotopes. Qualitative comparison in Fig 5.11 tells that calculation seems to produce more oblate states than prolate states. In the case of Rh-isotopes, there is only one strongly fed prolate final state. This results from the coupling of $5/2[413]d_{5/2}$ neutron state and $7/2[413]g_{9/2}$ proton state which results in an allowed unhindered-transition. If this would be a real case, then it would have been seen in the experiment. Instead of one very strong beta transition (order of magnitude faster than others) there appear at least two fast beta transitions and few other relatively fast ones. This suggest that the oblate distribution of the final state would describe better the experimentally obtained beta feeding pattern of the Ru-isotopes. In addition, the prolate final states tends to move to higher excitation energies when neutrons are added. Experimentally this has not been seen, which is against the assumption of the prolate shape of the Ru isotopes. $E_{ave}(1^+)$ comparison in Fig. 5.9 implies that either prolate nor oblate

calculations do not agree with experimental results. The deviation from the experimental results is smaller for the oblate calculations. In fact, for ^{110,112}Ru the prolate calculations produces all 1^+ final states above the experimental average energy. This suggest that prolate shape is not appropriate for the Ru-isotopes in question. In the case of ^{114}Ru comparison is complicated by the experimental difficulties related to the low production yield of very exotic ^{114}Ru. Result obtained do not rule out the possible γ-deformation. In the case of γ-deformation, the shape-hinderness of beta decay is reduced largely, but still beta decay is restricted between states having large shape deformation difference. It is also open question if there exist well defined minimum or γ-valley in a $\beta\gamma$-plane.

Mo-isotopes. In the case of Mo-isotopes, the situation reminds the Ru-isotopes with the exception that deformation energies are larger and deformations obtained are larger, too. On the contrary to Ru-isotopes, $E_{ave}(1^+)$ comparison clearly favors the prolate calculation over the oblate ones. In fact, the overall agreement between the experimental results and prolate calculations is very good as far as $E_{ave}(1^+)$ trend is concerned as shown in Fig. 5.10.
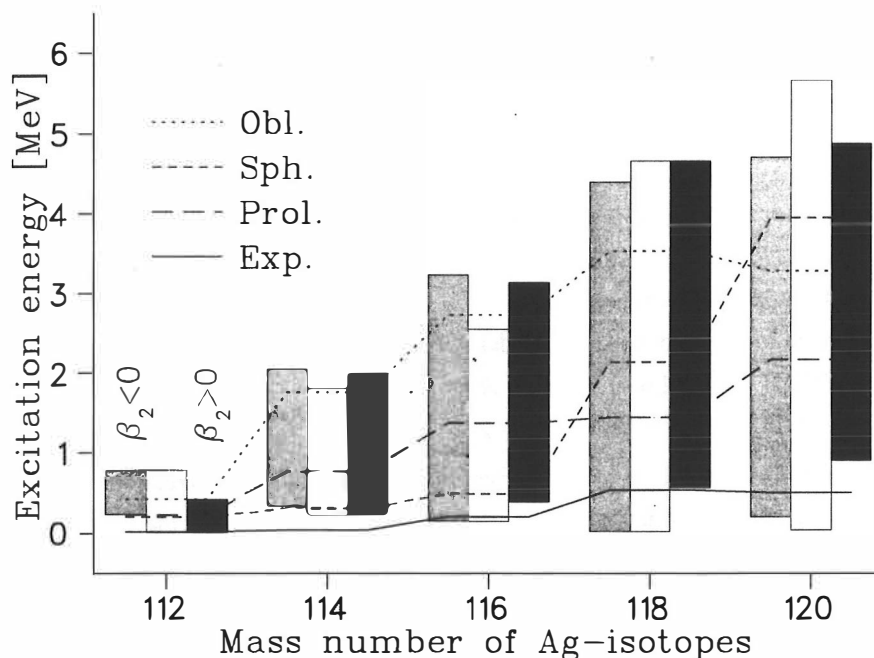
Figure 5.8 Comparison of the average energy of 1^+ states in the decay energy window for $^{114-120}$Pd- isotopes. Range of the oblate spherical and prolate 1^+ states are presented by the filled rectangles and the average energies of the states in different cases are presented by different lines as explained in the legend of the figure.
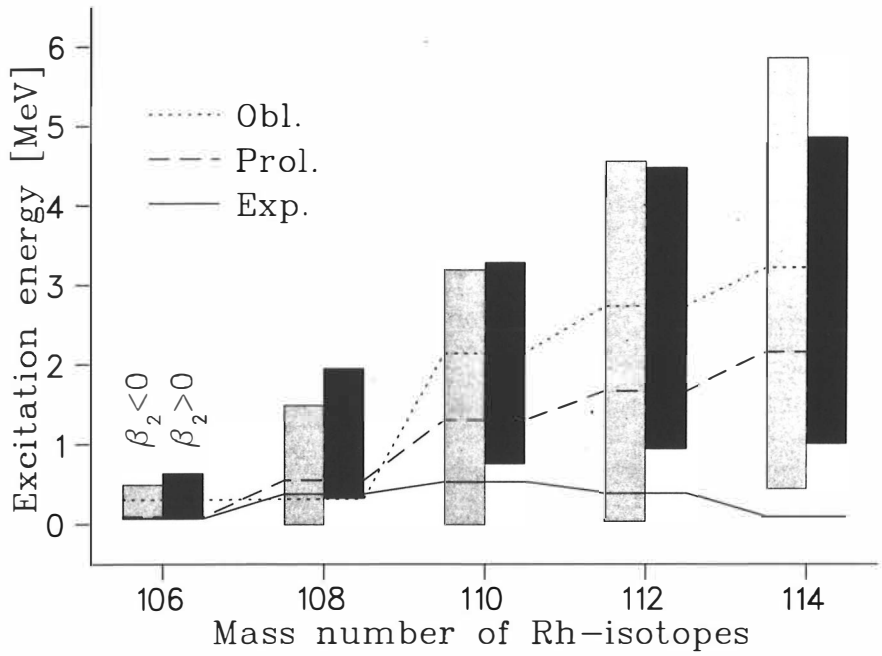
Figure 5.9 Comparison of the average energy of 1⁺ states in the decay energy window for
$^{106\text{-}114}$Ru-isotopes.
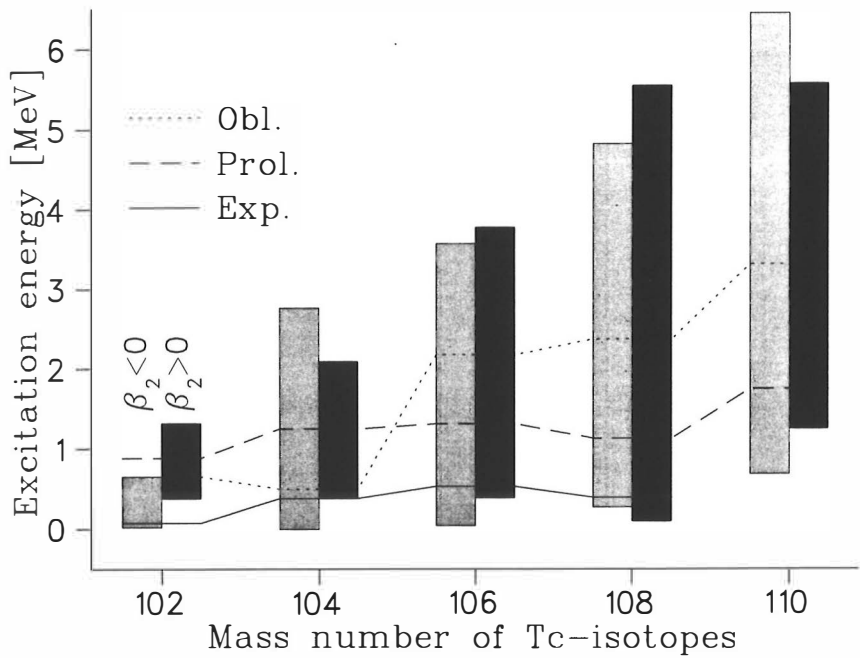
Figure 5.10 Comparison of the average energy of 1⁺ states in the decay energy window for
$^{102\text{-}110}$Mo-isotopes.
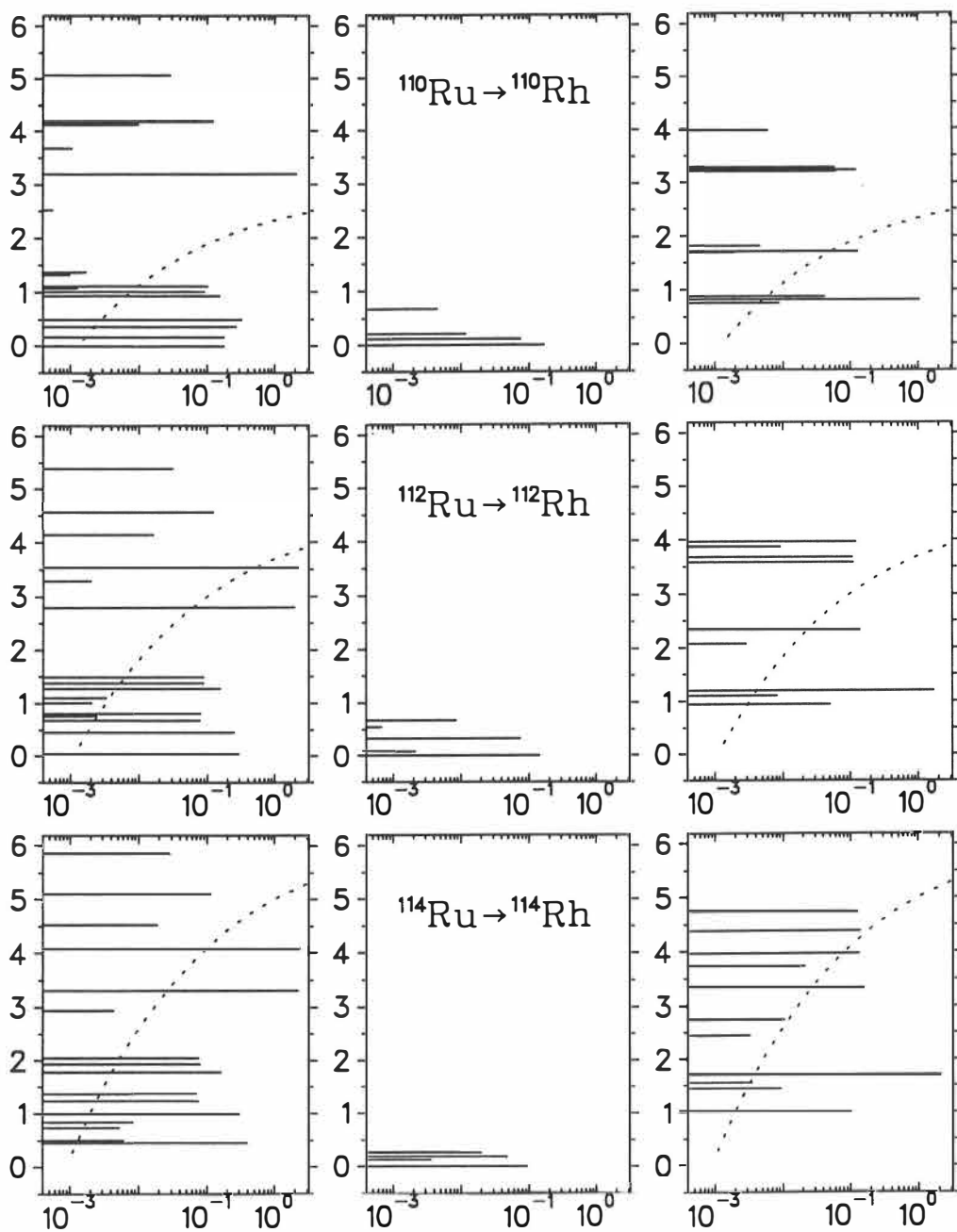
Figure 5.11 Calculated total GT-strength and observed beta-strength for $^{110\text{-}114}$Ru isotopes. Figures on the left and right correspond to calculated states with oblate and prolate deformations, respectively. Experimental distribution is presented in the middle. Figures on the left and right presents also curves corresponding to sensitivity limits equal to 0.5 % feeding of the state.
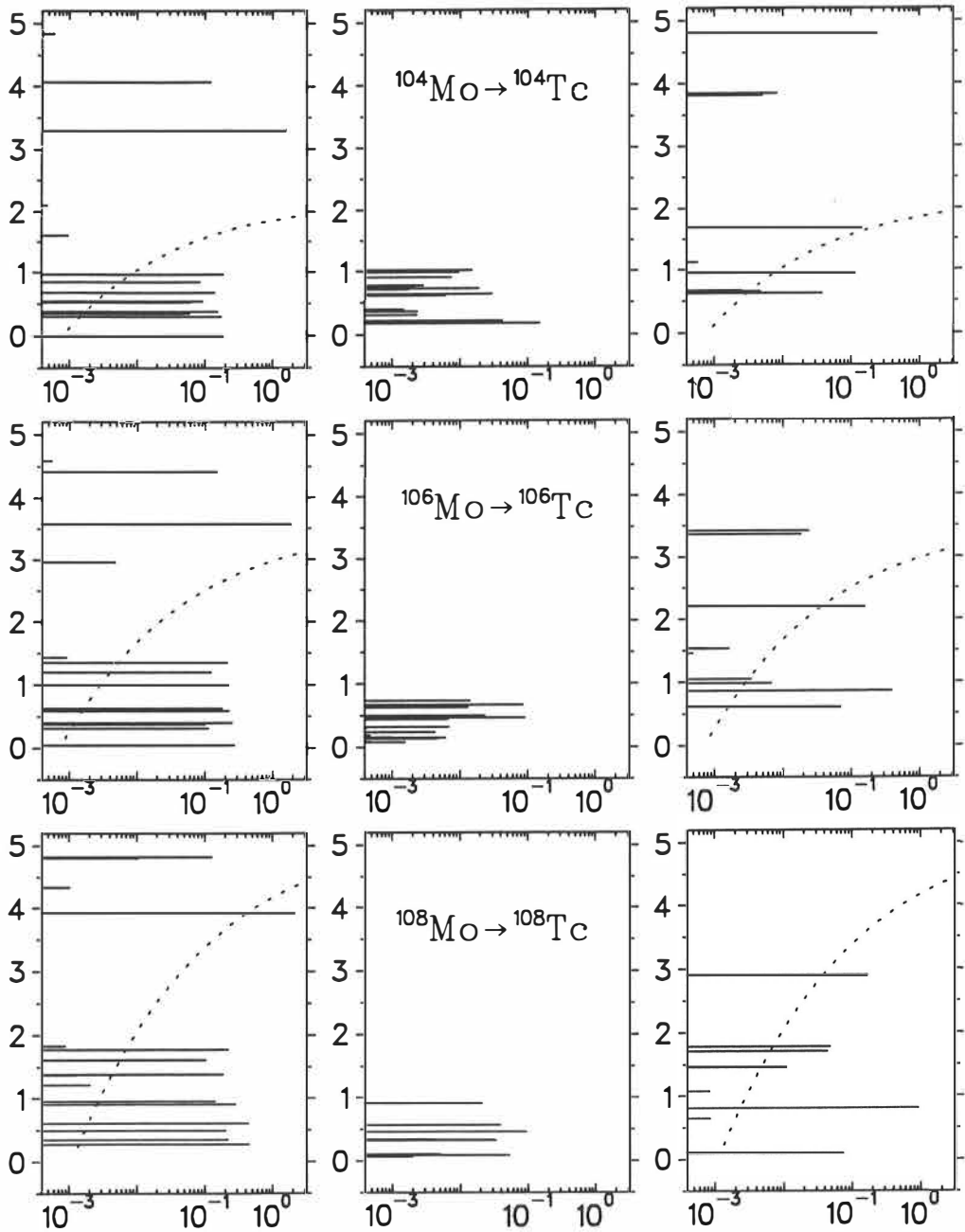
Figure 5.12 Calculated total GT-strength and observed beta-strength for $^{104-108}$Mo isotopes. Figures on the left and right correspond to calculated states with oblate and prolate deformations, respectively. Experimental distribution is presented in the middle. Figures on the left and right presents also curves corresponding to sensitivity limits equal to 0.5 % feeding of the state.

56

6 Summary

The experimental part of this work was conducted at the Department of Physics, University of Jyväskylä. A combination of the proton induced fission and the fast on-line mass separator IGISOL was applied in the study of neutron rich fission products. The radioactive decay of unstable nuclei was detected by using the beta-, gamma-, X-ray and conversion electron spectroscopic methods.

The studies of this thesis provided a vast amount of new experimental half-life and decay energy data for the neutron rich nuclei with $40 \leq Z \leq 46$ and A=105-120. Altogether seven new isotopes were identified. In the case of the even-even parent nuclei, beta decay properties were studied in greater. As a result the new decay schemes of ^{110,112,114}Ru and ^{108}Mo were constructed and the decay scheme of ^{106}Mo was revised.

The gross properties of allowed beta decay were compared to macroscopic-microscopic calculations as a possible indicator of the deformation of the nuclei. The Pd-isotopes are less deformed and characterized by the small deformation energies, which implies the competition of the different shapes. However, large values of an oblate deformation were ruled out in the comparison. Although the applied model could reproduce the decay energies of the Ru-isotopes reasonably well, the distribution of the Gamow Teller strength was not well reproduced. The results imply that neither oblate nor prolate deformation alone can explain the observed splitting and magnitude of the GT-strength. This leaves space for the γ-deformation, which is often associated to the Ru-isotopes. In the case of the Mo-isotopes, the comparison of the experimental and calculated distribution of the GT-strength implies the well developed prolate deformation of these nuclei.

The experimental results of fundamental beta decay properties were compared to various global models. Regarding the half-life predictions, the best agreement between the predictions and new experimental results was observed for the QRPA-model of Staudt *et al*. In the case of atomic mass predictions, all predictions agree reasonably well with experiments. However, information on nuclei with few more neutrons is needed for the stringent test for the atomic mass predictions presented in this work.

References

Abu92   Y. Aboussir, J.M. Pearson, A.K. Dutta, and F. Tondeur, Nucl. Phys. **A549** (1992) 155.

Ala55   G. Alaga, Phys. Rev. **100** (1955) 432.

Ale78   K. Aleklett, E. Lund, and G. Rudstam, Phys. Rev. C **18** (1978) 462.

Aud93   G. Audi, and A.H. Wapstra, Nucl. Phys. **A565** (1993) 1 and 66.

Bab71   S. Baba, H. Umezawa, and H. Baba, Nucl. Phys. **A175** (1971) 177.

Bal92   K. Balog, M. Graefenstedt, M. Groß, P. Jürgens, U. Keyser, F. Münnich, T. Otto, F. Schreiber, T. Winkelmann, J.Wulff, and the ISOLDE Collaboration, Z. Phys. **A342** (1992) 125.

Bla91   J. Blachot, Nucl. Data Sheets **64** (1991) 1.

Beh82   H. Behrens, and W. Bühring, *Electron Radial Wave Functions and Nuclear Beta-Decay*, (Clarendon Press, Oxford, 1982).

Ber90   M. Bernas, P. Armbruster, J.P. Bocquet, R. Brissot, H. Faust, Ch. Kozhuharov, and J.L. Sida, Z. Phys. **A336** (1990) 41.

Boh75   A. Bohr and B. Mottelson, *Nuclear structure*, Vols. I and II, (New York, Benjamin 1975).

Bol72   M. Bolsterli, E.O. Fiset, J.R. Nix, and J.L. Norton, Phys. Rev. C **5** (1972) 1050.

Bru77   P.J. Brussaard, and P.W.M. Glaudemans, *Shell Model Applications in Nuclear Spectroscopy,* (North Holland, Amsterdam, 1977).

Cas90   R.F. Casten, *Nuclear Structure from a Simple Prespective*, (Oxford University Press, New York, 1990).

Cha91   R.R. Chassman, Z. Phys. **A339** (1991) 111.

Coh71   B.L. Cohen, *Concepts of Nuclear Physics,* (McGraw-Hill, Inc., New York, 1971).

Com88   E. Comay, I. Kelson, and A. Zidon, At. Data Nucl. Data Tables **39** (1988) 235.

Cwi87   S. Cwiok, J. Dudek, W. Nazarewicz, J. Skalski, and T. Werner, Comp. Phys. Comm. **46** (1987) 379.

Dav58   A.S. Davydov, and G.F. Filippov, Nucl. Phys. **8** (1958) 237.

Dav76   C.N. Davids, E.B. Norman, R.C. Pardo, and L.A. Parks, Proceedings of the 3rd Conference on Nuclei far from Stability, Cargèse, 1976, R. Klapisch (ed.), Geneve, CERN 76-13, p. 590.

DeF88   D. De Frenne, E. Jacobs, M. Verboven, and G. De Smet, Nucl. Data Sheets **53** (1988) 73.

DeF89   D. De Frenne, E. Jacobs, and M. Verboven, Nucl. Data Sheets **57** (1989) 443.

DeF91   D. De Frenne, and E. Jacobs, Nucl. Data Sheets **63** (1991) 373.

DeG79   P. De Gelder, D. De Frenne, E. Jacobs, H. Thierens, A. De Clercq, P. D'hondt, A.J. Deruytter, F. Schussler, G. Tittel, N. Kaffrell, and N. Trautmann, Inst. Phys. Conf. Ser. No. **51** (1979) 297.

DeG83   P. De Gelder, E. Jacobs, D. De Frenne, Nucl. Data Sheets **38** (1983) 545.

Det89   C. Détraz, and D.J. Vieira, Ann. Rev. Nucl. Part. Sci. **39** (1989) 407.

Dob88   J. Dobaczewski, W. Nazarewicz, A. Plochocki, K. Rykaczewski, and J. Zylicz, Z. Phys. **A329** (1988) 267.

Dob94   J. Dobaczewski, I. Hamamoto, W. Nazarewicz, and J.A. Seikh, Phys. Rev. Lett. **72** (1994) 981

Dud79   J. Dudek, A. Majhofer, J. Skalski, T. Werner, S. Cwiok, and W. Nazarewicz, J. Phys. **G5** (1979) 1359.

Dud81   J. Dudek, Z. Szymánski, and T. Werner, Phys. Rev. C **23** (1981) 920.

Dud82   J. Dudek, Z. Szymánski, T. Werner, A. Faessler, and C. Lima, Phys. Rev. C **26** (1982) 1712.

Dur89   J.L. Durell, Inst. Phys. Conf. Ser. No. **105** (1989) 307.

Dus88   G. Dussel, E. Caurier, and A.P. Zuker, At. Data Nucl. Data Tables **39** (1988) 205.

Dut86   A.K. Dutta, J.-P. Arcoragi, J.M. Pearson, R. Behrman, and F. Tondeur, Nucl. Phys. **A458** (1986) 77.

Fog90   B. Fogelberg, Y. Zongyuan, B. Ekström, E. Lund, K. Aleklett, and L. Sihver, Z. Phys. **A337** (1990) 251.

Fra78   G. Franz, and G. Herrmann, J. Inorg. Nucl. Chem. **40** (1978) 945.

Fuj70   J.-I. Fujita, and G.T. Emery, Phys. Rev. C **1** (1970) 2060.

Gar66   G.T. Garvey and I. Kelson, Phys. Rev. Lett. **16** (1966) 197.

Gar69   G.T. Garvey, W.J. Gerace, R.L. Jaffe, I. Talmi, and I. Kelson, Rev. Mod. Phys **41** (1969) S1.

Gov71   N.B. Gove and M.J. Martin, At. Data Nucl. Data Tables **10** (1971) 205.

Gra86   M Graefenstedt, U. Keyser, F. Münnich, B. Pahlmann, B. Pfeiffer, and H. Weikard, Z. Phys. **A324** (1986) 15.

Gra87   M. Graefenstedt, U. Keyser, F. Münnich, F. Schreiber, H.R. Faust and, H. Weikard, Z. Phys. **A327** (1987) 383.

Gra89   M. Graefenstedt, P Jürgens, U. Keyser, F. Münnich, F. Schreiber, K. Balog, T. Winkelmann, and H.R. Faust, Z. Phys. **A334** (1989) 239.

Gra90   M. Graefenstedt, P Jürgens, U. Keyser, F. Münnich, F. Schreiber, K. Balog, T. Winkelmann, H.R. Faust, and B. Pfeiffer, Z. Phys. **A336** (1989) 247.

Gre87   R.C. Greenwood, R.A. Anderl, J.D. Cole, M.A. Lee, and H. Willmes, Paper presented at 5th International Conference on Nuclei Far From Stability, Rousseau Lake, Ontario, Canada, ed. Ian S. Towner, 1987, p.

Gro76   H.v. Groote, E.R. Hilf, and K. Takahashi, At. Data Nucl. Data Tables **17** (1976) 418.

Gro92   M. Groß, P. Jürgens, S. Kluge, M. Mehrtens, S. Müller, F. Münnich, and J. Wulff, Inst. Phys. Conf. Ser. **132** (1992) 77.

Han89   P.G. Hansen, and B. Jonson, in *Particle Emission from Nuclei III,* (CRC Press, Boca Raton, Florida, 1989), p. 157.

Hau88   P. Haustein, At. Data Nucl. Data Tables **39** (1988) 185.

Hil53   D.L. Hill, and J.A. Wheeler, Phys. Rev. **89** (1953) 1102.

Hil76   E.R. Hilf, H.v. Groote, and K. Takahashi, Proceedings of the Third International Conference on Nuclei far from Stability (CERN Report No. 76-13, 1976), p. 142.

Hot91   M.A.C. Hotchkis, J.L. Durell, J.B. Fitzgerald, A.S. Mowbray, W.R. Phillips, I. Ahmad, M.P. Carpenter, R.V.F. Janssens, T.L. Khoo, E.F. Moore, L.R. Morss, Ph. Benet, and D. Ye, Nucl. Phys. **A530** (1991) 111.

Jan93   Z. Janas, J. Äystö, K. Eskola, J. Kownacki, M. Leino, P.P. Jauho, A. Jokinen, J.M. Parmonen, H. Penttilä, J. Szerypo, and J. Zylicz, Nucl. Phys. **A552** (1993) 340.

Jau94   P.P. Jauho, A. Jokinen, M. Leino, J.M. Parmonen, H. Penttilä, J. Äystö, K. Eskola, and V.A. Rubchenya, JYFL Preprint 23/1993, Phys. Rev. C 1994, in press.

Jen84   A.S. Jensen, P.G. Hansen, and B. Jonson, Nucl. Phys. **A431** (1984) 393.

Jok91   A. Jokinen, J. Äystö, P. Dendooven, K. Eskola, Z. Janas, P.P. Jauho, M.E. Leino, J.M. Parmonen, H. Penttilä, K. Rykaczewski, and P. Taskinen, Z. Phys. **A340** (1991) 21.

Jok92   A. Jokinen, J. Äystö, K. Eskola, Z. Janas, P.P. Jauho, M. Leino, J.M. Parmonen, and H. Penttilä, Nucl. Phys. **A549** (1992) 420.

Jok92   A. Jokinen, J. Äystö, K. Eskola, T. Enqvist, Z. Janas, P.P. Jauho, M. Leino, J.M. Parmonen, H. Penttilä, and J. Zylicz, Paper presented at 6th International Conference on Nuclei Far From Stability & 9th International Conference on Atomic Masses and Fundamental Constants, Bernkastel-Kues, Germany, 1992. Inst. Phys. Conf. Ser. No 132: Section 5 (1992) 563.

Jok94   A. Jokinen, J. Äystö, K. Eskola, T. Enqvist, Z. Janas, P.P. Jauho, M. Leino, J.M. Parmonen, H. Penttilä, and J. Zylicz, submitted for publication to Nucl. Phys. A, 1994.

Jän88   J. Jänecke and P. Masson, At. Data Nucl. Data Tables **39** (1988) 265.

Kar91   E. Karttunen, M. Brenner, V.A Rubchena, S.A. Egorov, V.B. Funshtein, V.A. Jakovlev, and Yu.A. Selitkiy, Nucl. Sci. Eng. **109** (1991) 350.

Kla84   H.V. Klapdor, J. Metzinger, and T. Oda, At. Data Nucl. Data Tables **31** (1984) 81.

Kra93   K.-L. Kratz, J.-P. Bitouzet, F.-K. Thielemann, P. Möller and B. Pfeiffer, The Astrophysical Journal **403** (1993) 216.

Kop89   V. Koponen, J. Äystö, J. Honkanen, P. Jauho, H. Penttilä, J. Suhonen, P. Taskinen, K. Rykaczewski, J. Zylicz, and C.N. Davids, Z. Phys. **A333** (1989) 339.

Lei91   M. Leino, P.P. Jauho, J. Äystö, P. Dedrock, P. Dendooven, K. Eskola, M. Huyse, A. Jokinen, J.M. Parmonen, H. Penttilä, G. Reusen, P. Taskinen, P. Van Duppen, and J. Wauters, Phys. Rev. C **44** (1991) 336.

Lhe90   G. Lhersonneau, H. Gabelmann, N. Kaffrell, K.-L. Kratz, B. Pfeiffer, K. Heyde, and the ISOLDE-collaboration, Z. Phys. **A337** (1990) 143.

Lhe93   G. Lhersonneau, A. Jokinen, M. Leino, M. Huhta, J. Äystö, K.-L. Kratz, and A. Wöhr, Proposal to the ISOLDE-committee, 1993, unpublished.

Lia91   M. Liang, H. Ohm, B. De Sutter, K. Sistemich, B. Fazekas, and G. Mólnar, Z. Phys. **A340** (1991) 223.

Lip60   H.J. Lipkin, Ann. of Phys. **9** (1960) 272.

Mas88   P.J. Masson, and J. Jänecke, At. Data Nucl. Data Tables **39** (1988) 273.

Mei76   B.J. Meijer, Z. Phys. **A278** (1976) 365.

Mue94   A.C. Mueller, and B.M. Sherrill, to appear in Ann. Rev. Nucl. Part. Sci. **43** (1994).

Mye66   W.D. Myers, and W. Swiatecki, Nucl. Phys. **81** (1966) 1; Ark. Fys. **36** (1967) 343.

Möl81   P. Möller, and J.R. Nix, At. Data Nucl. Data Tables **26** (1981) 165.

Möl88a P. Möller, and J.R. Nix, At. Data Nucl. Data Tables **39** (1988) 213.

Möl88b P. Möller, W.D. Myers, W.J. Swiatecki, and J. Treiner, At. Data Nucl. Data Tables **39** (1988) 225.

Möl90   P. Möller, and J. Randrup, Nucl. Phys. **A514** (1990) 49.

Möl93   P. Möller, J.R. Nix, W.D. Myers and W.J. Swiatecki, submitted for publication to Nucl. Atomic Data and Nucl. Data Tables (1993).

Nil55   S.G. Nilsson, Mat. Fys. Medd. K. Dan. Vidensk. Selsk. **29**, no. 16 (1955).

Nog64   Y. Nogami, Phys. Rev. **134** (1964) B313

Ogl71   W. Ogle, S. Wahlborn, R. BJebJering, and S. Fredriksson, Rev. Mod. Phys. **43** (1971) 424.

Pah84   B. Pahlmann, M. Graefenstedt, U. Keyser, and F. Münnich, Z. Phys. **A318** (1984) 371.

Pap88   A. Pape, and M.S. Antony, At. Data Nucl. Data Tables **39** (1988) 201.

Par91   J.M. Parmonen, Z. Janas, W.H. Trzaska, J. Äystö, J. Kantele, P.P. Jauho, A. Jokinen and H. Penttilä, Nucl. Instr. Meth. Phys. Res. **A306** (1991) 504.

Pea91   J.M. Pearson, Y. Aboussir, A.K. Dutta, R.C. Nayak and M. Farine, Nucl. Phys. **A528** (528) 1.

Pen92   H. Penttilä, Ph.D. Thesis, University of Jyväskylä, 1992.

Phi94   W.R. Phillips, and J.L.Durell, private communication, to be published.

Pie62   W.R. Pierson, H.C. Griffin and C.D. Coryell, Phys. Rev. **127** (1962) 1708.

Pra73   H.C. Pradham, Y. Nogami, and J. Law, Nucl. Phys. **A201** (1973) 357.

Rav89   H.L. Ravn, and B.W. Allardyce, in *Treatise on Heavy Ion Science,* Vol. 8, ed. by D.A. Bromley, Plenum Press, New York, 1989), p. 363.

Rei71   W. Reisdorf, J.P. Unik, H.C. Griffin and L.E. Glendenin, Nucl. Phys. **A177** (1971) 337.

Roe92   E. Roeckl, Rep. Prog. Phys. **55** (1992) 1661.

Ros68   E. Rost, Phys. Lett. **B26** (1968) 184.

Ryk88   K. Rykaczewski, private communication.

Ryk89   K. Rykaczewski, K.-L. Gippert, N. Kaffrell, P. Kirchner, O. Klepper, V.T. Koslowsky, W. Kurcewicz, W. Nazarewicz, E. Roeckl, E. Runte, D. Schardt, W.-D. Schmidt-Ott, and P. Tidemand-Petersson, Nucl. Phys. **A499** (1989) 529.

Rös78   F. Rösel, H.M. Fries, K. Alder, and H.C. Pauli, At. Data Nucl. Data Tables **21** (1978) 91.

Sat88   L. Satpathy, and R.C. Nayak, At. Data Nucl. Data Tables **39** (1988) 241.

Sha94   M.M. Sharma, G.A. Lalazissis, W. Hillebrandt, and P. Ring, Phys. Rev. Lett. **72** (1994) 1431.

Ska80   G. Skarnemark, P.O. Aronsson, K. Brodén, J. Rydberg, T. Björnstad, N. Kaffrell, E. Stender, and N. Trautmann, Nucl. Instr. Meth. **171** (1980) 323.

Sol76   V.G. Soloviev, *Theory of Complex Nuclei* (Pergamon Press, 1976).

Soo89   P.C. Sood, At. Data Nucl. Data Tables **43** (1989) 259.

Soo90   P.C. Sood, and R.K. Sheline, Phys. Scripta Vol. **42** (1990) 25.

Soo92   P.C. Sood, and R.K. Sheline, Proc. Int. Symp. on "Spectroscopy and Structure of Molecules and Nuclei", Tallahassee, Florida, 1992, p. 69.

Spa87   L. Spanier, K. Aleklett, B. Ekström, and B. Fogelberg, Nucl. Phys. **A474** (1987) 359.

Spa88   L. Spanier, and S.A.E. Johansson, At. Data Nucl. Data Tables **39** (1988) 259.

Suh88   J. Suhonen, T. Taigel, and T. Faessler, Nucl. Phys. **A486** (1988) 91.

Suh92   J. Suhonen and O. Civitarese, Phys. Lett. **B280** (1992) 191.

Süm80   K. Sümmerer, N. Kaffrell, E. Stender, N. Trautmann, K. Brodén, G. Skarnemark, T. Björnstad, I. Haldorsen, and J.A. Maruhn, Nucl. Phys. **A339** (1980) 74.

Sta84   J. Stachel, N. Kaffrell, N. Trautmann, K. Brodén, G. Skarnemark, and D. Eriksen, Z. Phys. **A316** (1984) 105.

Sta89   A. Staudt, E. Bender, K. Muto, and H.V. Klapdor, Z. Phys. **A334** (1989) 47.

Sta90   A. Staudt, E. Bender, K. Muto, and H.V. Klapdor-Kleingrothaus, Atomic Data Nucl. Data Tables **44** (1990) 79.

Str67   V.M. Strutinsky, Nucl. Phys. **A96** (1967) 420.

Str68   V.M. Strutinsky, Nucl. Phys. **A122** (1968) 1.

Stö90   U. Stöhlker, A. Blönningen, W. Lippert, and H. Wollnik, Z. Phys. **A336** (1990) 374.

Tac88a   T. Tachibana, S. Ohsugi, and M. Yamada, Proceedings of 5th International Conference on Nuclei far from Stability, Rosseau Lake, Canada, I. Towner (ed.), AIP Conf. Proc. 164, AIP, New York, 1988, p. 558.

Tac88b   T. Tachibana, M. Uno, M. Yamada, and S. Yamada, At. Data Nucl. Data Tables **39** (1988) 251.

Tak73   K. Takahashi, M. Yamada and T. Kondoh, At. Data Nucl. Data Tables **12** (1973) 101.

Tan85   I. Tanihata, H. Hamagaki, O. Hashimoto, Y. Shida, N. Yoshikawa, K. Sugimoto, O. Yamakawa, T. Kobayashi, N. Takahashi, Phys. Rev. Lett. **55** (1985) 2676.

Tan91   I. Tanihata, in *Treatise on Heavy-Ion Science,* Vol 8, ed. D.A. Bromley, (Plenum,New York, 1989), p. 443

Tas89   P. Taskinen, H. Penttilä, J. Äystö, P. Dendooven, P. Jauho, A. Jokinen, and M. Yoshii, Nucl. Instr. Meth. in Phys. Res. **A281** (1989) 539.

Thi91   F.K. Thielemann, and K.-L. Kratz, Synthesis of Nuclei in Astrophysical Environments, in Proceedings of the 22nd Mikolajki Summer School, 1991.

Ton87   F. Tondeur, A.K. Dutta, J.M. Pearson and R. Behrman, Nucl. Phys. **A470** (1987) 93.

Tow85   I.S. Towner, Nucl. Phys. **A444** (1985) 402.

Trz89   W.H. Trzaska, Ph.D. Thesis, University of Jyväskylä, 1989.

Uno80   M. Uno and M. Yamada, in Atomic Masses and Fundamental Constants, edited by J.A. Nolen,Jr., and W. Benenson, (Plenum, New York, 1980) p. 141.

Uno81   M. Uno, and M. Yamada, Prog. Theor. Phys. **65** (1981) 1322.

Wah88   A.C. Wahl, At. Data Nucl. Data Tables **39** (1988) 1.

Wap77   A.H. Wapstra, and K. Bos, At. Data Nucl. Data Tables **19** (1977) 175; **20** (1977) 1.

Wap85   A.H. Wapstra, and G. Audi, Nucl. Phys. **A432** (1985) 1 and 55.

Wap88   A.H. Wapstra, G. Audi, and R. Hoekstra, At. Data Nucl. Data Tables **39** (1988) 281.

Van73   R. Vandenbosch, and J.R. Huizenga, Nuclear Fission (Academic, New York, 1973).

Wil56   L. Wilets, and M. Jean, Phys. Rev. C **102** (1956) 788.

Vir90   A. Virtanen, Ph.D. Thesis, University of Jyväskylä, Finland, 1990.

Vol89   V.V. Volkov, in *Treatise on Heavy Ion Science,* Vol. 8, ed. by D.A. Bromley, (Plenum Press, New York, 1989), p. 101.

Zyl66   J. Zylicz, P.G. Hansen, H.L. Nielsen, and K. Wilsky, Ark. Fys. **36** (1966) 643.

Ärj87   J. Ärje, J. Äystö, P. Taskinen, J. Honkanen, and K. Valli, Nucl. Instr. and Meth. **B26** (1987) 384.

Äys87   J. Äystö, P. Taskinen, M. Yoshii, J. Honkanen, P. Jauho, J. Ärje, and K. Valli, Nucl. Instr. and Meth. **B26** (1987) 394.

Äys88   J. Äystö, C.N. Davids, J. Hattula, J. Honkanen, K. Honkanen, P. Jauho, R. Julin, S. Juutinen, J. Kumpulainen, T. Lönnroth, A. Pakkanen, A. Passoja, H. Penttilä, P. Taskinen, E. Verho, A. Virtanen, and M. Yoshii, Nucl. Phys. **A480** (1988) 104.

Äys89   J. Äystö, and J. Cerny, in *Treatise on Heavy-Ion Science,* Vol 8, ed. D.A. Bromley, (Plenum,New York, 1989), p. 207

Äys90   J. Äystö, P.P. Jauho, Z. Janas, A. Jokinen, J.M. Parmonen, H. Penttilä, P. Taskinen, R. Béraud, R. Duffait, A. Emsallem, J. Meyer, M. Meyer, N. Redon, M.E. Leino, K. Eskola, and P. Dendooven, Nucl. Phys. **A515** (1990) 365.

Äys92   J. Äystö, A. Astier, T. Enqvist, K. Eskola, Z. Janas, A. Jokinen, K.-L. Kratz, M. Leino, H. Penttilä, B. Pfeiffer, and J. Zylicz, Phys Rev. Lett. **69** (1992) 1167.

Appendices

A1 Half-live analysis based on the intensity ratio of growth-in and decay periods

In the case of a very low production yield, it is possible to estimate the half-life of the decaying nucleus by using the ratio of observed intensities in a growth-in and decay period. The method is sensitive to the choice of the length of the growth-in and decay periods compared to the half-life of the decay. If a decay rate of the nucleus is λ and the length of the growth-in period is X and the length of the decay period is YX then the number of the observed decay events in the first period is integral of the growth-in formula:

$$I_1 = \int_0^X N(1-\exp(-\lambda t))dt = NX + \frac{N}{\lambda}(\exp(-\lambda X)-1) \qquad (A1.1)$$

In the decay period the corresponding integral is

$$I_2 = \int_0^{YX} N_0 \exp(-\lambda t)dt = \frac{N}{\lambda}(\exp(-\lambda X)-1)(\exp(-\lambda YX)-1) \qquad (A1.2)$$

The ratio of the above mentioned integrals,

$$\frac{I_1}{I_2} = \frac{\lambda X + \exp(-\lambda X)-1}{(\exp(-\lambda X)-1)(\exp(-\lambda YX)-1)} \qquad (A1.3)$$

depends only on the decay rate λ and the lengths X and YX of the growth-in and decay periods. The value of a ratio can be deduced from the gamma-spectra collected both in the growth-in and decay periods. With this information, the decay rate λ is obtained from equation (A1.3) by iteration.

A2 Estimation of the ground state branching of the beta decay by using the radioactive decay laws for the decay chain

Let's assume that nucleus 1 is produced directly by fission with production a yield Y_1 and it decays with a decay rate λ_1. Its daughter, nucleus 2, having a decay rate λ_2 is also produced in fission with a production yield of Y_2. Additionally, nucleus 2 is produced via the decay of nucleus 1. Due to the steep fall off of the production yield far from the stability, the production of the parent of the nucleus 1 can be neglected, which simplifies the formulation of the problem. The growth-in period starts at $t=0$ and ends at $t=T'$. The decay period lasts from $t = T'$ to $t = T$.

Differential equations for the nuclei 1 and 2 in the growth-in period ($0 \le t \le T'$) are

$$\frac{dN_1}{dt} = Y_1 - \lambda_1 N_1 \qquad\qquad ; N_1(0) = 0 \tag{A2.1}$$

$$\frac{dN_2}{dt} = Y_2 + \lambda_1 N_1 - \lambda_2 N_2 \qquad ; N_2(0) = 0 \tag{A2.2}$$

and similarly for the decay period ($T' \le t \le T$)

$$\frac{dN_1}{dt} = -\lambda_1 N_1 \qquad\qquad ; N_1(0) = n_{01} \tag{A2.3}$$

$$\frac{dN_2}{dt} = -\lambda_2 N_2 + \lambda_1 N_1 \qquad ; N_2(0) = n_{02} \tag{A2.4}$$

with boundary conditions following each equations. All these equations can be solved analytically leading to the following expressions of the activities observed.

Growth-in period:

$$A_1(t) = Y_1 \big[1 - \exp(-\lambda_1 t) \big] \tag{A2.5}$$

$$A_2(t) = Y_1 \big[1 - \exp(-\lambda_2 t) \big] + Y_2 \big[1 - \exp(-\lambda_2 t) \big] -$$
$$Y_1 \frac{\lambda_2}{\lambda_2 - \lambda_1} \big[\exp(-\lambda_1 t) - \exp(-\lambda_2 t) \big] \tag{A2.6}$$

Decay period:

$$A_1(t) = n_{01} \exp(-\lambda_1 t) \tag{A2.7}$$

$$A_2(t) = A_{02} \exp(-\lambda_2 t) + A_{01} \frac{\lambda_1 \lambda_2}{\lambda_1 - \lambda_2} \big[\exp(\lambda_2 t) - \exp(\lambda_1 t) \big] \tag{A2.8}$$

where $A_{01} = A_1(t = T')$ and $A_{02} = A_2(t = T')$.

The values of A_{01} and A_{02} can be fitted for the decay of the daughter nucleus by applying Eq. (A2.8). After fitting the A_{01} and A_{02}, the production yields Y_1 and Y_2 of the nuclei can be obtained from the Eqs. (A2.5) and (A2.6). When all variables are known the ratio of the total number of decays of the nuclei 1 and 2 can be calculated by integrating the Eqs. (A2.5)-(A2.8) over the measurement cycle. The total number of the decays of nucleus 1 is obtained by using the ratio determined and the observed number of the decays of nucleus 2. The ground state branching of the nucleus 1 is then obtained from the difference of the total number of decays and the observed feeding of the excited states. This method has been used in this work for example in the case of ^{112}Ru in Paper I. Figure 4 of Paper I presents the decay curve of 777.5 keV transition in ^{112}Pd during the decay period corresponding to Eq. (A2.8).